

## Keynotes

- Stereology: personal recollections . . . . . 9  
*Luis M. Cruz-Orive (University of Cantabria)*
- Finding Hyperuniformity – a Hidden Order among Disorder . . . . . 9  
*Michael A. Klatt (Princeton University)*
- Graphical Monte Carlo and permutation tests for functions and images . . . 10  
*Mari Myllymäki (Natural Resources Institute Finland)*
- Modeling Temporally Evolving and Spatially Globally Dependent Data . . . 10  
*Emilio Porcu (Newcastle University)*
- 3D image analysis in material science with particular focus on fiber reinforced composites . . . . . 11  
*Katja Schladitz (Fraunhofer ITWM, Kaiserslautern)*
- Three Dimensional Electron Microscopy Imaging Technology in Life Sciences 11  
*Fei Sun (Chinese Academy of Sciences)*

## Talks

- Gibbsian T-tessellation model for agricultural landscape . . . . . 14  
*Katarzyna Adamczyk-Chauvat (INRA)*
- A Morphological Transform to Increase Geometric Invariance and Generalization in Convolutional Neural Networks . . . . . 14  
*Jesús Angulo (MINES ParisTech)*
- Characterization of pore connectivity using geodesic paths . . . . . 15  
*Sandra Barman (Chalmers University of Technology)*
- Pruning neural networks thanks to morphological layers . . . . . 17  
*Samy Blusseau (MINES ParisTech)*
- Extensions of the  $M$ -tortuosity for heterogeneity assessment and grayscale images characterization . . . . . 17  
*J. Chaniot (IFP Energies nouvelles; Université de Lyon, Université Jean Monnet de Saint Etienne)*

Sparse models for highly multivariate log-Gaussian Cox processes . . . . .	19
<i>Achmad Choiruddin (Aalborg University)</i>	
Design unbiased population size estimation . . . . .	19
<i>Marcos Cruz (Universidad de Cantabria)</i>	
Detecting and tracking myelinated axons in volumetric data . . . . .	20
<i>Vedrana A. Dahl (Technical University of Denmark)</i>	
Recent Advances in Deep Neural Networks with Morphological Operators to Improve Semantic Segmentation of Histological Images . . . . .	21
<i>Etienne Decencière (MINES ParisTech)</i>	
Fitting 3D model to polycrystalline alloys based on 2D micrographs . . . . .	22
<i>Dascha Dobrovolskij (Hochschule Darmstadt and Fraunhofer ITWM)</i>	
The History of the Cavalieri Estimator – Post, Present, and Future . . . . .	23
<i>Karl-Anton Dorph-Petersen (Aarhus University; University of Pittsburgh)</i>	
Local Minkowski measures for random set geometrical characterization. . .	24
<i>Tatyana Eremina (MINES Saint-Étienne)</i>	
Eikonal-based models of random tessellations . . . . .	26
<i>Bruno Figliuzzi (MINES ParisTech)</i>	
Extraction of poorly visible grain boundaries from tomographic image data, using convolutional neural networks . . . . .	27
<i>Orkun Furat (Ulm University)</i>	
A Stereological Study of the Dopaminergic Innervation and its Targets in the Human Amygdaloid complex . . . . .	28
<i>M. García-Amado (Universidad Autónoma de Madrid)</i>	
Investigating the lung with 3D images from light and electron microscopy	29
<i>Roman Grothausmann</i>	
Imaging Brain Fibers with Diffusion MRI . . . . .	30
<i>Tom Dela Haije (University of Copenhagen)</i>	
Stochastic Modeling of Fiber-reinforced Ultra High Performance Concrete based on 3D Image Analysis . . . . .	30
<i>Konstantin Hauch (TU Kaiserslautern)</i>	
Similarity of realisations of random sets via approximation by unions of convex compact sets . . . . .	32
<i>Kateřina Helisová (Czech Technical University in Prague)</i>	
The detection of subtle changes in 3D microstructural relations in the CNS using 2nd order stereological methods measured with isotropic linear rulers.	32
<i>C. Vyvyan Howard (University of Ulster)</i>	

Possibilities of virtual reality approach for measurement and 3D visualization of tubular microstructures . . . . .	34
<i>Lucie Kubínová (Czech Academy of Sciences)</i>	
The Benefits of Digital Pathology . . . . .	35
<i>Arvydas Laurinavičius (Vilnius University Hospital)</i>	
Orientation maps from gray-level images using oriented granulometry . . .	35
<i>David Legland (INRA)</i>	
Estimation of absolute number of alveolar epithelial type 2 cells in mouse lungs: a comparison between stereology and flow cytometry . . . . .	36
<i>Rory E. Morty (Max Planck Institute for Heart and Lung Research)</i>	
Deep learning in pathology . . . . .	37
<i>Mads Nielsen (University of Copenhagen)</i>	
State of the art EM techniques for quantitative assessment of lung structure	37
<i>Matthias Ochs (Charité – Universitaetsmedizin Berlin; German Center for Lung Research)</i>	
Changes in midbrain dopaminergic circuitry in the maternal immune activation rat model of schizophrenia: ultrastructural stereological analyses	38
<i>D.E. Oorschot (University of Otago)</i>	
Information depth in backscattered scanning electron microscopy . . . . .	39
<i>Johannes A. Österreicher (Austrian Institute of Technology)</i>	
Limit theorems for random marked tessellations . . . . .	39
<i>Zbyněk Pawlas (Charles University)</i>	
Assessing in vivo neuronal reprogramming by automated, resonance-scanned confocal virtual tissue image acquisition and artificial intelligence-assisted stereology . . . . .	40
<i>Daniel A. Peterson (Rosalind Franklin University of Medicine and Science)</i>	
Recognition of meadow saffron sites in drone images, using a machine-learning approach . . . . .	41
<i>Lukas Petrich (Ulm University)</i>	
Stochastic 3D microstructure modeling of differently compacted cathodes in lithium-ion batteries . . . . .	41
<i>Benedikt Prifling (Ulm University)</i>	
Quality assurance of digital image analysis by stereological estimation using stratified sampling . . . . .	43
<i>Allan Rasmusson (Vilnius University)</i>	
Quantitative microscopy for characterizing material microstructures and mass transport . . . . .	44
<i>Magnus Röding (RISE Research Institutes of Sweden)</i>	

Quantifying the influence of 3D microstructure on effective conductivity and permeability of composite and porous materials . . . . .	45
<i>Volker Schmidt (Ulm University)</i>	
Applications of Gibbs-Laguerre tessellations to the modeling of polycrystalline materials . . . . .	46
<i>Filip Seitzl (Charles University)</i>	
3D microstructure and heterogeneous strain response of cemented carbides during deformation . . . . .	46
<i>Xiaoyan Song (Beijing University of Technology)</i>	
A generalization of Ripley's $K$ -function for space curves . . . . .	47
<i>Jon Sporring (University of Copenhagen)</i>	
Similarity of realisations of random sets via their morphological skeletons	47
<i>Jakub Staněk (Charles University)</i>	
Asymptotic Variance of Newton-Cotes Quadratures based on Randomized Sampling Points . . . . .	47
<i>Mads Stehr (CSGB)</i>	
Digital pathology – what to come in the future . . . . .	48
<i>Torben Steiniche (Aarhus University Hospital)</i>	
Hard of Listening: Auditory Cortex Pathology in Schizophrenia (Stereologically (Un?) Informed Studies of Auditory Cortex in Schizophrenia) . . . . .	48
<i>Robert A. Sweet (University of Pittsburgh)</i>	
Effects of fluoxetine on the cognitive function, neurons and synapses in the hippocampus of APP/PS1 transgenic mouse model of Alzheimer's disease .	49
<i>Yong Tang (Chongqing Medical University)</i>	
On approximating mathematical morphology operators via deep learning techniques . . . . .	51
<i>Santiago Velasco-Forero (MINES ParisTech)</i>	
Atomically Accurate 3D Measurements on Nanometer-size Structures by HR-SEM and Modeling . . . . .	51
<i>András E. Vladár (NIST)</i>	
Automatic detection of amyloid fibril crossovers in cryo-EM image data, using a combination of conventional image processing and machine learning	53
<i>Matthias Weber (Ulm University)</i>	
Reconstruction and stochastic 3D modeling of grain boundaries in polycrystalline materials from incomplete data, using tessellations with flat and curved facets . . . . .	54
<i>Daniel Westhoff (Ulm University)</i>	

Pronofrut: IT-assisted Stereology for Monitoring Orchards for Precision  
Horticulture . . . . . 55  
*Dvoralai Wulfsohn (Geco Enterprises Centro de I+D; Dayenu Ltda)*

## Posters

GABA(A) receptor $\alpha 3$ subunit deficit in the prefrontal cortex of Df(h22q11)/+ genetic mouse model of schizophrenia . . . . .	58
<i>Abdel-Rahman Al-Absi (Aarhus University; CSGB)</i>	
Effects of combined angiotensin II receptor antagonism and neprilysin inhibition in experimental pulmonary hypertension and right ventricular failure . . . . .	58
<i>Stine Andersen (Aarhus University Hospital)</i>	
Determination of Sample Size for Counting Podocytes using the Fractionator/Disector . . . . .	59
<i>John M. Basgen (Charles R. Drew University of Medicine and Science)</i>	
Hippocampal volume and cell number in depression, schizophrenia, and suicide subjects . . . . .	65
<i>Fenghua Chen (Aarhus University)</i>	
Measuring an angle of the curvature of the spine with scoliosis on X-rays images . . . . .	66
<i>Aneta Gądek-Moszczak (Cracow University of Technology)</i>	
GABAergic system deficit in the prefrontal cortex of Df(h15q13)/+ genetic mouse model of schizophrenia . . . . .	67
<i>Cecilie Josefine Mørch Ingkirk (Aarhus University)</i>	
Does Olanzapine change Orexin A expression? . . . . .	68
<i>Mia Staal Jensen (Aarhus University)</i>	
Statistical aspects of random tessellations with microstructure marks . . . . .	69
<i>Iva Karafiátová (Charles University)</i>	
Classification task in the context of replicated point patterns . . . . .	69
<i>Kateřina Koňasová (Charles University, Prague)</i>	
Characterisation of minicoloumnarity and volume tensors of neurons in Brodmann Area 46 in normal, schizophrenic and depressive human autopsy brains . . . . .	70
<i>Nick Y. Larsen (Aarhus University)</i>	
Morphological Dynamics of the Regenerative Hepatocyte . . . . .	70
<i>Michelle Meier (Aarhus University Hospital)</i>	
Does Olanzapine leads to changes in the hypothalamic opioid system? . . . . .	75
<i>Maiken K. Mikkelsen (Aarhus University)</i>	
Quantification of histopathological changes in the inner ear and electrophysiological assessment of hearing function in newborn piglets with hypoxic-ischemic-encephalopathy following perinatal asphyxia . . . . .	76
<i>Rebecca Nyengaard (Aarhus University)</i>	

Pathological changes in the cerebellum of patients with Multiple System Atrophy and Parkinson's disease . . . . .	77
<i>Mikkel V. Olesen (Bispebjerg and Frederiksberg Hospital)</i>	
Identifying structural endophenotypes in a rat model of schizophrenia-like behavior . . . . .	77
<i>Estrid Thougard Pedersen (RLSN, Bispebjerg and Frederiksberg Hospital)</i>	
Evaluation of Corneal confocal microscopy images in patients with type 1 diabetes and diabetic polyneuropathy: a stereological reappraisal . . . . .	78
<i>Ellen Lund Schaldemose (Aarhus University Hospital)</i>	
Superficial dorsal horn volume loss in dogs with neuropathic pain and syringomyelia – a quantitative and qualitative histological characterisation of cervical spinal cord lesions . . . . .	79
<i>Maria Søndergaard Thøfner (University of Copenhagen)</i>	
Covering of the realisations of the random sets . . . . .	80
<i>Markéta Zikmundová</i>	

# **Part I**

## **Keynotes**

Luis M. Cruz-Orive (University of Cantabria)

***Stereology: personal recollections***

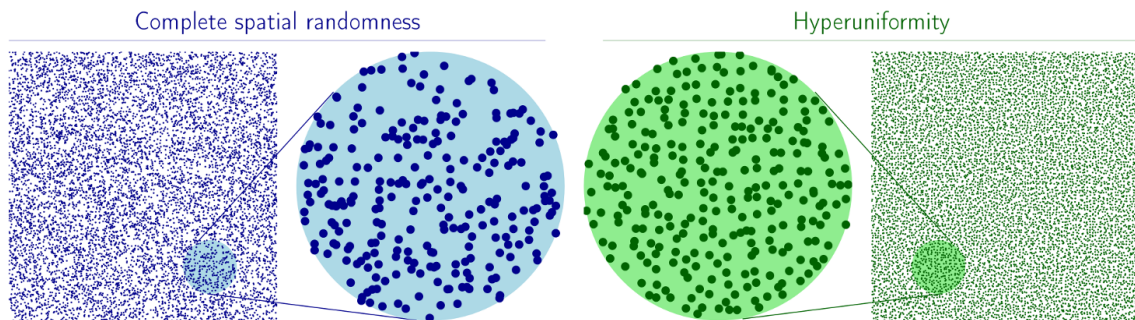
My purpose is to present a few personal recollections relevant to the evolution of stereology from the beginning of my academic career in the early 1970's, to date. Technical details were given in [1], hence the presentation is informal, and subjected to personal biases affecting any witness. In some sense, the underlying story was one of missed opportunities: the implementation of important results that 'were there' at a given time was often delayed for many years. The interaction between teachers and participants at the international ISS courses played a decisive role in the emergence of 'assumption free' stereology.

*References*

- [1] Cruz-Orive LM (2017). Stereology: a historical survey. *Image Anal Stereol* 36, 153–177.

Michael A. Klatt (Princeton University)

***Finding Hyperuniformity – a Hidden Order among Disorder***



From the eyes of chicken to exotic many-particle ensembles and random matrices, the concept of hyperuniformity has shed light on a variety of seemingly unrelated fields. It is defined as the anomalous suppression of density fluctuations on large length scales [1]. For disordered structures, this implies a hidden order such that the system remains macroscopically uniform, despite not being crystalline.

The unique properties of hyperuniform amorphous materials have recently led to intense research in physics, mathematics, material science, and biology; for example, see [2,3,4]. Aiming for an intuitive understanding of the rigorous mathematical definitions, this talk presents both basic concepts and recent examples.

Motivating that questions concerning hyperuniformity naturally arise in stereology, an outlook addresses questions of ongoing research: How can hyperuniformity be detected from cross sections that are themselves not hyperuniform? Can hyperuniformity be attained in cross sections of different dimensions?

*References*

- [1] Torquato, Stillinger. *Physical Review E*, 68 (2003)

- [2] Ghosh, Lebowitz. *Indian J. Pure Appl. Math.* 48 (2017)
- [3] Torquato. *Physics Reports*, 745 (2018)
- [4] Klatt, Last, Yogeshwaran. *arXiv:1810.00265* (2018)

Mari Myllymäki (Natural Resources Institute Finland)

***Graphical Monte Carlo and permutation tests for functions and images***

Global envelopes are useful for graphical interpretation of the results in Monte Carlo and permutation tests based on functional or multivariate statistics. They have shown their usefulness already in many areas, e.g. in spatial statistics, functional data analysis, image and point pattern analysis with applications to ecology, neuroscience, forestry, economics, geography, material science, eye movement research etc. Graphical Monte Carlo goodness-of-fit tests are used particularly in spatial statistics, where the data are highly complex statistical objects, e.g. point patterns or random sets, and test statistics are one-dimensional functions. The global envelopes can however be defined for a general multivariate vector, i.e. for a function of any dimensions and also for an image, and the tested hypothesis extend beyond goodness-of-fit testing. This talk describes the global envelopes and shows their use also in graphical permutation tests for functions or images, including functional ANOVA and general linear model (GLM).

Emilio Porcu (Newcastle University)

***Modeling Temporally Evolving and Spatially Globally Dependent Data***

*Joint with Alfredo Alegria and Reinhard Furrer*

The last decades have seen an unprecedented increase in the availability of data sets that are inherently global and temporally evolving, from remotely sensed networks to climate model ensembles. This paper provides an overview of statistical modeling techniques for space–time processes, where space is the sphere representing our planet. In particular, we make a distinction between (a) second order-based approaches and (b) practical approaches to modeling temporally evolving global processes. The former approaches are based on the specification of a class of space–time covariance functions, with space being the two-dimensional sphere. The latter are based on explicit description of the dynamics of the space–time process, that is, by specifying its evolution as a function of its past history with added spatially dependent noise.

We focus primarily on approach (a), for which the literature has been sparse. We provide new models of space–time covariance functions for random fields defined on spheres cross time. Practical approaches (b) are also discussed, with special emphasis on models built directly on the sphere, without projecting spherical coordinates onto the plane.

We present a case study focused on the analysis of air pollution from the 2015 wildfires in Equatorial Asia, an event that was classified as the year's worst environmental disaster. The paper finishes with a list of the main theoretical and applied research problems in the area, where we expect the statistical community to engage over the next decade.

Katja Schladitz (Fraunhofer ITWM, Kaiserslautern)

***3D image analysis in material science with particular focus on fiber reinforced composites***

*Joint with Dascha Dobrovolskij, Joachim Ohse and Oliver Wirjadi*

The development of modern high-performance materials requires a deeper understanding of the complex relations between a material's micro-structure geometry and its macroscopic properties. Quantitative image analysis combined with stochastic micro-structure modelling is a promising approach to study these relations. A key ingredient for this is a reliable geometric description provided by the quantitative analysis of 3D images of the materials micro-structures. This talk gives an overview over methods for characterizing structures based on spatial image data as obtained e. g. by micro computed tomography. Particular attention is paid to algorithms that rely on segmentation of the component to be analyzed but do not require to further separate it into individual image objects.

Fiber reinforced composites are a class of materials gaining more and more attraction due to their potential in lightweight design. This potential is nevertheless often not fully exploited since fiber distribution and orientation are on the one hand crucial for the reinforcement to serve its purpose and on the other hand hard to monitor non-destructively throughout the processing chain. Here, we review the state of the art for estimating the spatial local fiber orientation. The fiber orientation distribution is defined on the unit sphere and is therefore preferably estimated based on fully three-dimensional images of the microstructure.

Fei Sun (Chinese Academy of Sciences)

***Three Dimensional Electron Microscopy Imaging Technology in Life Sciences***

Biological electron microscopy has gone into a new era with great advances of specimen preparation, instrumentation and data processing. With the three dimensional reconstruction technique, the three dimensional electron microscopy (3DEM) has been becoming important approaches to image the biological system in high resolution and multiple scales. Based on the principle of the methodology itself, 3DEM can be classified into several categories to meet different needs from structural biology to cell biology, developmental biology and neuron sciences. In this talk, I will summarize my personal view of different 3DEM techniques and then introduce the relevant technology developments in our biological imaging center.

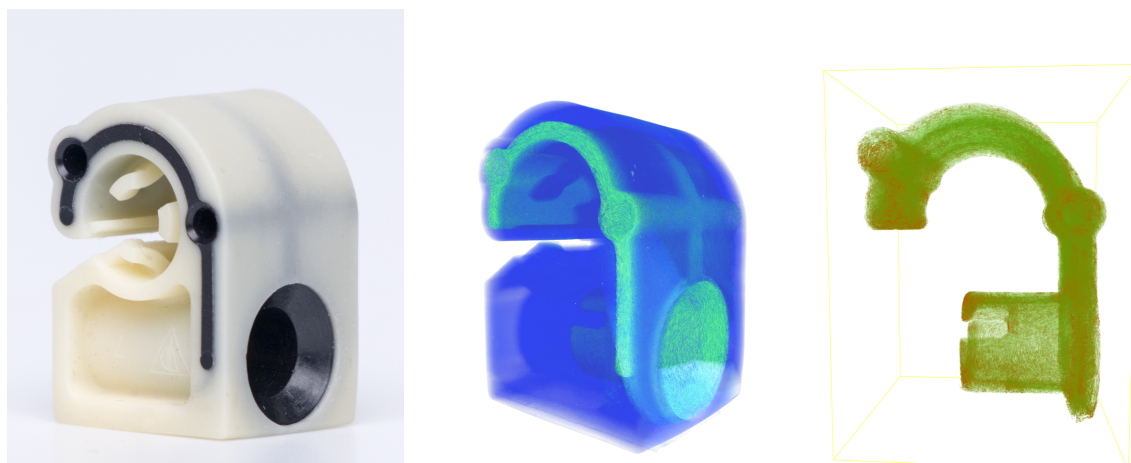


**Figure 1:** Brake pipe clip made from glass fibre reinforced polymer, imaged by micro computed tomography at  $12.5\ \mu\text{m}$  voxel size. Picture (left), volume rendering with fiber component in green (center), and volume rendering of xx-component of the 2nd order orientation tensor estimated in cubic subvolumes of edge length  $250\ \mu\text{m}$  (right, green – low xx-component, red – high xx-component).

### References

- [1] Li X., Zhang S., Zhang J. and Sun F. (2018), In situ protein micro-crystal fabrication by cryo-FIB for electron diffraction. *Biophysics Reports* 4(6): 339–347.
- [2] Li S., Ji G., Shi Y., Klausen L.H., Niu T., Wang S., Huang X., Ding W., Zhang X., Dong M., Xu W., and Sun F. (2018), High-vacuum optical platform for cryo-CLEM(HOPE): a new solution for non-integrated multiscale correlative light and electron microscopy. *Journal of Structural Biology*, 201(1): 63–75.
- [3] Li X., Ji G., Chen X., Ding W., Sun L., Xu W., Han H., and Sun F. (2017), Large scale three-dimensional reconstruction of an entire *Caenorhabditis elegans* larva using AutoCUTS-SEM. *Journal of Structural Biology*, 200(2): 87–96.
- [4] Shi, Y., Wang, L., Zhang, J., Zhai, Y. and Sun F. (2017) Determining the target protein localization in 3D using the combination of FIB-SEM and APEX2, *Biophysics Reports*. 3, 92–99.
- [5] Deng Y., Chen Y., Zhang Y., Wang S., Zhang F. and Sun F. (2016), ICON: 3D reconstruction with ‘missing-information’ restoration in biological electron tomography. *Journal of Structural Biology* 195(1): 100–112.
- [6] Zhang J., Ji G., Huang X., Xu W. and Sun F. (2016), An improved cryo-FIB method for fabrication of frozen hydrated lamella. *Journal of Structural Biology* 194(2): 218–223.
- [7] Han R., Wang L., Liu Z., Sun F. and Zhang F. (2015), A novel fully automatic scheme for fiducial marker-based alignment in electron tomography. *Journal of Structural Biology* 192: 403–17.

# **Part II**

## **Talks**

Katarzyna Adamczyk-Chauvat (INRA)

***Gibbsian T-tessellation model for agricultural landscape***

*Joint with Mouna Kassa and Radu S. Stoica*

Gibbsian T-tessellation model [1] is based on an energy function involving a set of tessellation statistics. Depending on the selected statistics the model can control various T-tessellation features. This property of the model can be applied in modelling and simulating agricultural landscape patterns.

We propose a model for agricultural landscape controlling the number of cells, the metrics related to cells shape and size as well as the proportion of edges types. We illustrate the model fit on a French landscape example. The original data set is first approximated by a T-tessellation. We apply MCML method [2] to calculate model parameters. Model assessment is based on the comparison of the empty-space distance distribution for the observed pattern and model simulations.

*References*

- [1] K. Kiêu, K. Adamczyk-Chauvat, H. Monod, R.S. Stoica (2013). A completely random T-tessellation model and Gibbsian extensions. *Spatial Statistics*, 6:118-138.
- [2] C.J. Geyer (1994). On the convergence of Monte Carlo Maximum Likelihood calculations. *J. R. Statist. Soc. B* , 56(3):261-274.

Jesús Angulo (MINES ParisTech)

***A Morphological Transform to Increase Geometric Invariance and Generalization in Convolutional Neural Networks***

*Joint with Santiago Velasco-Forero*

Convolutional Neural Networks are nowadays one of the most useful paradigms in deep learning and provide significant state-of-the-art results on image classification and image/object segmentation. A suitable mathematical theory of deep convolutional neural networks (DCNN) for feature extraction has been considered previously [2, 7], in particular concerning the robustness and geometric invariance (i.e., sensitivity to image deformation).

Distance function is a classical transform to represent a shape as a function which provides an extended morphological description since its level sets are associated to isotropic erosions and dilations of the shape. Distance function has been used in several DCNN architectures for object segmentation and shape classification [5, 6].

Our goal is to theoretically justify the interest of the distance function to increase the geometric invariance in DCNN for feature extraction from general images in classification tasks. Firstly, we review the morphological and stochastic

properties of the Molchanov distance function (MDF) [3], which is the natural extension of the distance transform for gray-scale images. Secondly, we prove our result of Lipschitz stability and deformation sensitivity bound of DCNN descriptors, in the case where these descriptors are learnt from images represented by their MDF. Thirdly, we provide some experiments to illustrate the performance and robustness of classification after image perturbation. Additionally, we consider the behavior of our morphological representation based on the MDF vs. the original image representation against adversarial attacks [1, 4].

### References

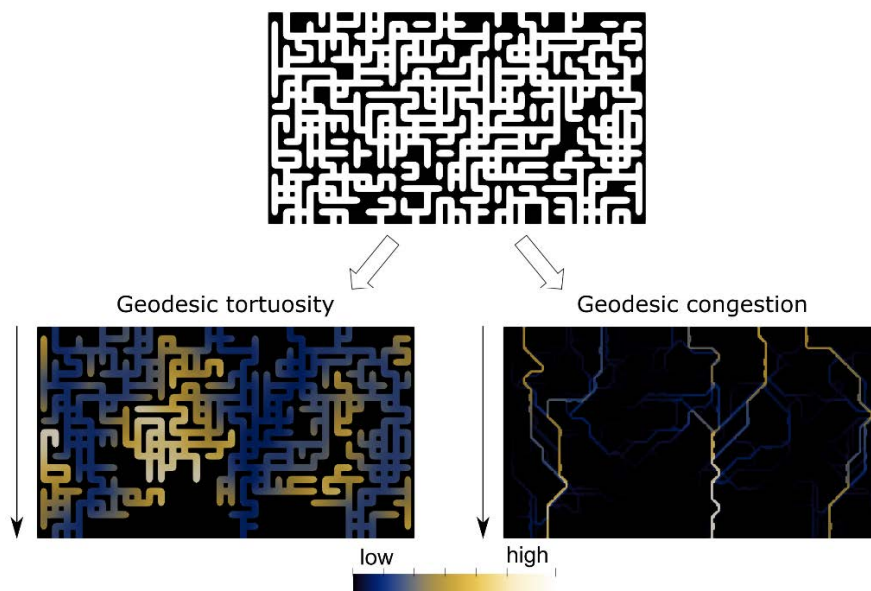
- [1] I. Goodfellow and J. Shlens and Ch. Szegedy. Explaining and Harnessing Adversarial Examples. *International Conference on Learning Representations (ICML'15)*, 2015.
- [2] S. Mallat. Understanding deep convolutional networks. *Philosophical Transactions of the Royal Society A: Mathematical, Physical and Engineering Sciences*, Vol. 374, Issue 2065, 2016.
- [3] I.S. Molchanov, P. Terán. Distance transforms for real-valued functions. *Journal of Mathematical Analysis and Applications*, Vol. 278, 472–484, 2003.
- [4] S.M. Moosavi-Dezfooli, A. Fawzi, P. Frossard. Deepfool: a simple and accurate method to fool deep neural networks. In *Proc. IEEE CVPR'16*, 2016.
- [5] P. Naylor, M. Laé, F. Reyat, T. Walter. Segmentation of Nuclei in Histopathology Images by deep regression of the distance map. *IEEE Trans. on Medical Imaging*, Vol. 38, No. 2, 448–459, 2019.
- [6] J.J. Park, P. Florence, J. Straub, R. Newcombe, S. Lovegrove. DeepSDF: Learning Continuous Signed Distance Functions for Shape Representation. In *Proc. IEEE CVPR'19*, 2019.
- [7] T. Wiatowski, H. Bölcskei. A mathematical theory of deep convolutional neural networks for feature extraction. *IEEE Trans. on Information Theory*, Vol. 64, No. 3, 1845–1866, 2018.

Sandra Barman (Chalmers University of Technology)

### *Characterization of pore connectivity using geodesic paths*

To understand macroscopic properties of a porous material – such as diffusive transport, heat transfer, electrical conductivity, fluid permeability and mechanical strength – it is important to be able to quantify aspects of the pore geometry that influence the macroscopic property of interest. One such aspect is the connectivity of the pore network, which can be quantified using so called geodesic paths through the pore system. A geodesic path in this context is a shortest path that connects a point in the pore system to both the inlet and the outlet. The length of a geodesic path is called the geodesic tortuosity. This path-length measure has been shown to be a very good predictor of diffusive transport [1, 2] (and thus also of heat transfer and electrical conductivity since the governing equations are

equivalent), especially if the geodesic tortuosity is computed for the whole pore network [2] as in the 2-D example shown in the figure below. We develop new methods for characterizing and visualizing the connectivity of the pore geometry based on geodesic paths. For characterization, we develop a measure that captures large scale bottleneck effects in the pore network. Our new measure, called geodesic congestion [3] (see the figure below), counts how many geodesic paths pass through each point in the pore space and thus captures bottlenecks caused by path congestion. Bottlenecks are an important factor influencing diffusive transport, and bottlenecks caused by variations in pore size have previously been shown to perform well as a predictor of diffusive transport [1]. For visualization, we compute geodesic paths starting at a specific pore and divide the paths into categories by length. The categories are visualized separately, giving an idea of how the pore network is connected which can be difficult to find from just visual inspection of a 3-D pore network [4].



### References

- [1] O. Stenzel, O. Pecho, L. Holzer, M. Neumann, and V. Schmidt. Predicting effective conductivities based on geometric microstructure characteristics. *AIChE Journal*, 62:1834–1843, 2016.
- [2] S. Barman, H. Rootzén, and D. Bolin. Prediction of diffusive transport through polymer films from characteristics of the pore geometry. *AIChE Journal*, 65(1):446–457, 2018.
- [3] S. Barman, C. Fager, M. Röding, A. Olsson, N. Lorén, C. von Corswant, E. Olsson, A. Särkkä, D. Bolin and H. Rootzén. Characterization of Pore Shape and Connectivity of Coatings used for Controlled Drug Release. Manuscript.
- [4] C. Fager, S. Barman, M. Röding, A. Olsson, N. Lorén, C. von Corswant, E. Olsson, A. Särkkä, D. Bolin and H. Rootzén. 3D Visualisation of Transport Paths in Coatings for Controlled Drug Release using FIB-SEM. Manuscript.

Samy Blusseau (MINES ParisTech)

***Pruning neural networks thanks to morphological layers***

*Joint with Yunxiang Zhang, Santiago Velasco-Forero, Isabelle Bloch and Jesús Angulo*

Motivated by recent advances in morphological neural networks, we further study the properties of morphological units when incorporated in layers of conventional neural networks. We confirm and extend the observation that a Max-plus layer can be used to select relevant filters and reduce redundancy in its previous layer, without incurring performance loss. We present several experiments in image processing, showing that this filter selection property seems efficient and robust. We also point out the close connection between Maxout networks and our pruned Max-plus networks. The code related to our experiments is available online (<https://github.com/yunxiangzhang>).

J. Chaniot (IFP Energies nouvelles; Université de Lyon, Université Jean Monnet de Saint Etienne)

***Extensions of the M-tortuosity for heterogeneity assessment and grayscale images characterization***

*Joint with M. Moreaud, L. Sorbier, D. Jeulin, T. Fournel and J.-M. Becker*

Tortuosity is among the foremost of the topological descriptors. Unfortunately, it has not a simple or universal definition [1–2]. We propose two new topological descriptors based on geometric tortuosity notion [3], more specifically based on the *M-tortuosity* concept [4]. First, by using the *M-tortuosity* formalism to quantify heterogeneity and second, by extending its definition to gray-level images. *M-tortuosity* descriptor already handles disconnections in complex interconnected microstructures without definition of arbitrary entry and exit. Our descriptors are named *H-tortuosity* and *F-tortuosity*, respectively. Both are based on Monte Carlo method, the first one uses dilating spheres to assess an overall geometric tortuosity value for a given distance. The second descriptor uses the functional definition of geodesic distance transform [5–6]. The particularity of the *F-tortuosity* is that the functional geodesic distance  $FD_G$  is used as a guide into the grayscale maze, for the computation of the *projected functional geodesic distance*  $FD_G^\perp$ , defined as the length of the shortest path on the grayscale image, orthogonally projected on the hyperplane of intensity equal to zero.

$N$  points  $p_n$  are sampled in the image such that  $p_n \neq c$ , the center of mass of the porous volume. For each pair  $(p_n, p_m)$ , the *functional geometric tortuosity*  $\tau_{f_{n,m}}$  is computed as being the ratio of  $FD_G^\perp$  and their Euclidean distance  $D$ . The *F-coefficient*  $C_{f_n}$ , attached to the starting point  $p_n$ , is defined as in [4] using the harmonic mean of  $\{\tau_{f_{n,m}}\}_{m \in \llbracket 0, N-1 \rrbracket, m \neq n}$  weighted by the inverse of their respective geodesic distances. Finally, the *F-scalar*  $\tau_F$  is defined, according to [4], as the harmonic mean of  $\{C_{f_n}^{-1}\}_{n \in \llbracket 0, N-1 \rrbracket}$  weighted by the inverse of their respective Euclidean

distances to  $c$ . The extension is possible thanks to  $FD_G$ ,

$$FD_G(p_m, p_n; I) = \inf_{\Gamma_f \in \gamma_{f_{p_n, p_m}}} \int_{p_n}^{p_m} \sqrt{1 + (I'(S))^2} ds$$

with  $\gamma_{f_{p_n, p_m}}$  the set of all paths between  $p_n$  and  $p_m$  constrained by gray-levels of  $I, \Gamma_f$  one of these paths and  $s$  the arc length.  $FD_G$  is used to compute  $FD_G^\perp$  defined as,

$$FD_G^\perp(p_m, p_n; I) = L(\Gamma^*) \quad \text{with, } \Gamma^* = (\Gamma_f^*)_\perp$$

with  $\Gamma^*$  the orthogonal projection of the shortest path  $\Gamma_f^*$  on the hyperplane of intensity equal to zero and  $L(\Gamma^*)$  the length of  $\Gamma^*$ . Such a formulation makes possible the characterization of unsegmented images.

The *F-tortuosity* applied on the distance transform (cf. Fig. 1 (d)) of a binary image, allows to combine tortuosity notion with narrowness, highlighting bottleneck effect. Validation and results of both descriptors, on several multi-scale Boolean schemes [7–10] will be shown (cf, Fig. 1). Their discriminant power will be pointed out. Finally, application on alumina catalyst supports, obtained by electron tomography, will be presented.

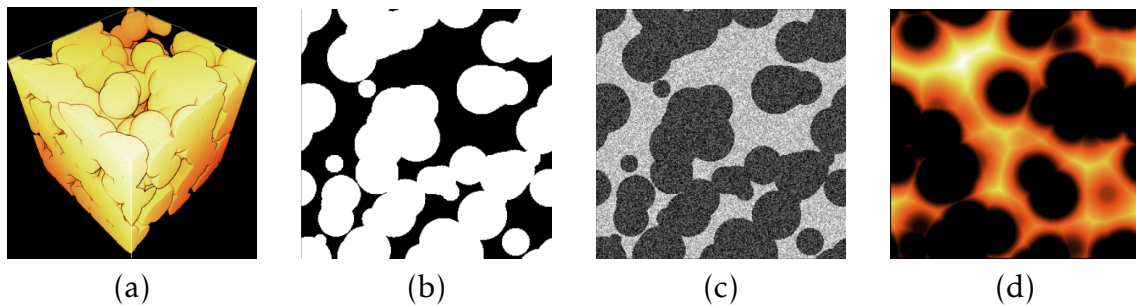


**Figure 1:** (a) 3D visualization of Boolean scheme of spheres (radius = 30, volume fraction = 0.7), (b-c) slice of (a) for reference value computation (b) and validation on noisy image (c), (d) slice of (a) of 3D geodesic distance map from the spheres boundary.

## References

- [1] M.B. Clennell (1997). *Tortuosity: a guide through the maze*. Geological Society, London, Special Publications 122(1):299–344.
- [2] B. Ghanbarian, A.G. Hunt, R.P. Ewing, M. Sahimi (2013). *Tortuosity in porous media: a critical review*. Soil Science Society of America, Inc., 77(5):1461–1477.
- [3] C. Lantuéjoul, S. Beucher (1981). *On the use of the geodesic metric in image analysis*. Journal of Microscopy, Wiley Online Library, 121(1):39–49.
- [4] J. Chaniot, M. Moreaud, L. Sorbier, J.-M. Becker, T. Fournel (2019). *Tortuosimetric operator for complex porous media characterization*. Image Analysis & Stereology, to be published.
- [5] A. Rosenfeld, J.L. Pfaltz (1968). *Distance Functionson Digital Pictures*. Pattern Recognition 1:33–61.

- [6] L. Ikonen, P. Toivanen (2007). *Distance and nearest neighbor transforms on gray-level surfaces*. Pattern Recognition Letters, 28(5):604–612.
- [7] G. Matheron (1975). *Random sets and integral geometry*. J. Wiley, New York.
- [8] D. Jeulin, M. Moreaud (2006). *Percolation of multi-scale fiber aggregates*. S4G (Stereology, Spatial Statistics and Stochastic Geometry) 6th International Conference, Prague, Czech republic.
- [9] S.N. Chui, D. Stoyan, W.S. Kendall, J. Mecke (2013). *Stochastic geometry and its applications*. John Wiley & Sons.
- [10] H. Wang, F. Willot, M. Moreaud, M. Rivallan, L. Sorbier, D. Jeulin (2017). *Modeling hindered diffusion in  $\gamma$ -alumina catalyst supports*. Oil & Gas Science and Technology.

Achmad Choiruddin (Aalborg University)

***Sparse models for highly multivariate log-Gaussian Cox processes***

*Joint with Rasmus Waagepetersen, Francisco Cuevas-Pachecho and Jean-François Coeurjolly*

Statistical inference for highly multivariate point pattern data is very challenging due to complex models with large numbers of parameters. In this study we develop numerically stable and efficient parameter estimation methodology by introducing regularization and using convex optimization algorithms for a class of multivariate log Gaussian Cox processes. The methodology is applied to a highly multivariate point pattern data set from tropical rain forest ecology.

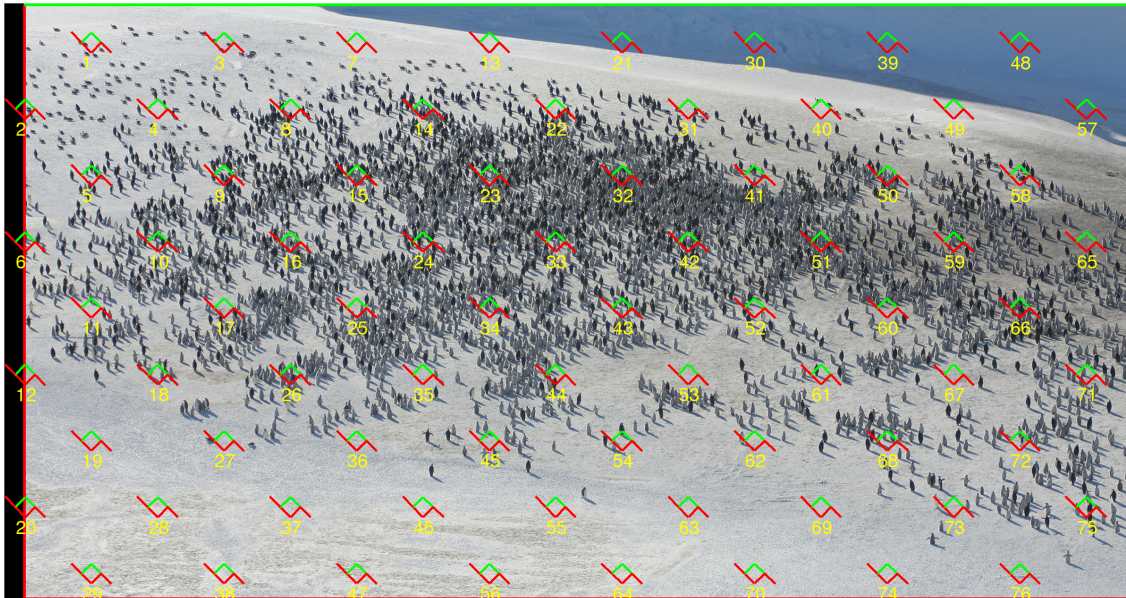
Marcos Cruz (Universidad de Cantabria)

***Design unbiased population size estimation***

*Joint with Javier González-Villa*

Population sizing is essential in ecological and social sciences and relevant to many real world applications such as demonstrations, political rallies, concerts, marathons, etc. Manual counting on images is slow, tedious and observer dependent, while automatic computer recognition methods are biased and are known to fail for large populations. We proposed ([1]) a design unbiased method, based on geometric sampling principles which are largely unknown outside the areas of three dimensional microscopy and stereology. The performance of the method was checked on 51 manually annotated images with population sizes between 96 and 4633 ([2]). The relative standard error was shown to be in the 5%–10% range through automatic Monte Carlo replicated sampling on the manually annotated positions. In addition we proposed a variance estimator which contemplates quadrat dependence using the Cavalieri slices design ([4]). In [3] we show how to reduce the variance caused by inhomogeneous population patterns that arise in

gigapixel images due to perspective artifacts. The source code and software of the method are available at <http://countem.unican.es>.



### References

- [1] Cruz M, Gómez D, Cruz-Orive LM (2015). Efficient and Unbiased Estimation of Population Size. PLoS ONE 10(11):e0141868. doi:10.1371/journal.pone.0141868.
- [2] Cruz, M., & González-Villa, J. (2018a). Simplified procedure for efficient and unbiased population size estimation. PLoS ONE 13(10): e0206091.
- [3] Cruz, M., & González-Villa, J. (2018b). Unbiased Population Size Estimation on Still Gigapixel Images (OnlineFirst). *Sociological Methods & Research*, Doi: 10.1177/0049124118799373.
- [4] Gómez AI, Cruz M, Cruz-Orive LM (2019). Variance prediction for population size estimation. Submitted to IAS.

Vedrana A. Dahl (Technical University of Denmark)

### ***Detecting and tracking myelinated axons in volumetric data***

*From a work with Lars Dahlin, Martin Bech, Martin Kjer and Anders Dahl*

Advances in tomography allow us to visualize the 3D fibre micro-structure of a tissue. We are often interested in whether a disease affects the tissue and changes its micro-structure. Such hypothesized correlation is exemplified in following questions: Does diabetes influence the radius, trajectory and organization of myelinated axons in human peripheral nerves? Does cerebral palsy influence the size and the muscle fibres and the micro-architecture of the muscle tissue?

In these questions, the hypothesized change in the fibre micro-structure is subtle and can not be revealed by visual inspection, or by conducting measurements in only a few places. Therefore, automated methods leading to quantification of fibre radius, trajectory and organization are required for establishing the correlation between the fibre micro-structure and the disease.

The focus of this talk is an automated method developed for segmenting, tracking and measuring myelinated axons in human peripheral nerves, see Fig. 1. This method employs a geometric representation of the segmented axon, making the method robust to noise often present in 3D tomography. Geometric representation is also favorable for a subsequent quantification of the fibre micro-structure. With small modifications, the method has also been used for tracking muscle cells, and for tracking myelinated axons in brain tissue.

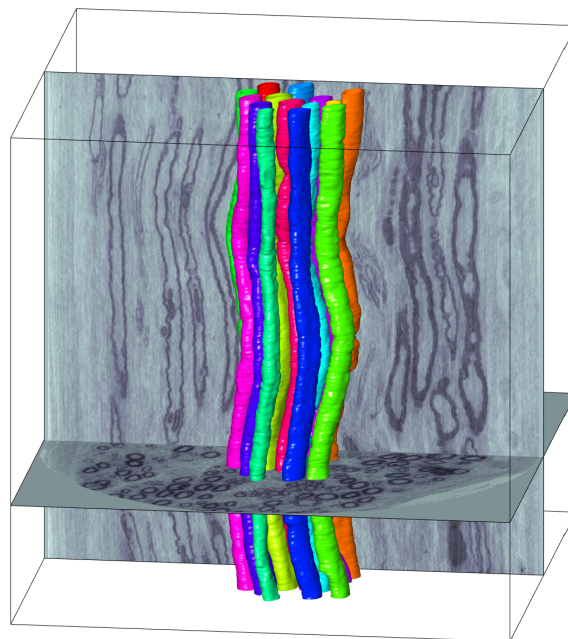


**Figure 1:** A cluster of tracked axons is shown together with two orthogonal slices through the volumetric data of a human peripheral nerve.

Etienne Decencière (MINES ParisTech)

***Recent Advances in Deep Neural Networks with Morphological Operators to Improve Semantic Segmentation of Histological Images***

*Joint with Santiago Velasco-Forero, Virginie Flouret, Catherine Cohen, Thomas Bornschlöggl and Thérèse Baldeweck*

The present study aims at automatically quantifying the melanin pigment on histological images from cross-sections of reconstructed human skin after Fontana Masson staining, in order to evaluate pro- or de-pigmenting potential of cosmetic

ingredients. Whole Slide Imaging (WSI) allows acquiring a large number of large field-of-view images with millions of pixels, such that image processing becomes essential. Given that melanin is to be quantified within each skin compartment, the first processing step consists in the segmentation of the different skin layers: stratum corneum, living epidermis and living dermis (3 interfaces to be detected). However, due to the variability of experimental conditions, images aspect and color characteristics can change between studies or samples. The challenge of this study was to perform a robust segmentation even if the tissue and/or the acquisition conditions are different.

Deep neural networks (DNNs) for semantic segmentation of color-stained histological images constitute an active topic of research. The use of fully convolutional networks allows applying models to images of varying sizes which is convenient in histopathology image analysis. In this context, segmentation is considered as an image-to-image transform. This transform can be learnt by training DNNs architectures such as U-net [1]. However, these methods require a sufficient number of images to cover the variability encountered in image acquisition. To overcome this issue, many authors have explored preprocessing techniques, multi-resolution decomposition and/or data-augmentation techniques to facilitate the training of DNNs.

Three main contributions are presented in this paper. At first, the implementation of a new random sampling protocol for on-the-fly training; Second, improvements to the standard U-net architecture and, Third the inclusion of morphological layers in this U-net architecture to take into consideration prior information about the shape/size of objects to be detected in the image. These modifications are well suited to handle the large variability within the data. Using the proposed on-the-fly training protocol allows us to learn a model that performs much better than competing methods even on a heterogeneous image database.

### *References*

- [1] O. Ronneberger, P. Fischer, and T. Brox. "U-net: Convolutional networks for biomedical image segmentation." MICCAI, pp. 234–241, 2015.

Dascha Dobrovolskij (Hochschule Darmstadt and Fraunhofer ITWM)

### ***Fitting 3D model to polycrystalline alloys based on 2D micrographs***

*Joint with Claudia Redenbach*

Many components are made of polycrystalline alloys featuring a cellular microstructure of particular interest in various applications, e. g. the study of mechanical properties, propagation of microscopical cracks, and non-destructive testing of components by ultrasound techniques. In all these applications, the studied phenomena depend on the spatial distribution and on the shape distribution of

the cells. [1] studied an  $\alpha$ -titanium alloy and stated the grain size of this polycrystalline alloy to be log-normally distributed. [2] suggested a Laguerre-tessellation based on dense non-overlapping sphere packings as an adequate model. In any case, if the 3D model is to be fit on exclusively 2D information, one runs into an ill-posed problem. We approach this problem by iterative adaptation of the cell number and comparing the achieved results based on extracted 2D sections.

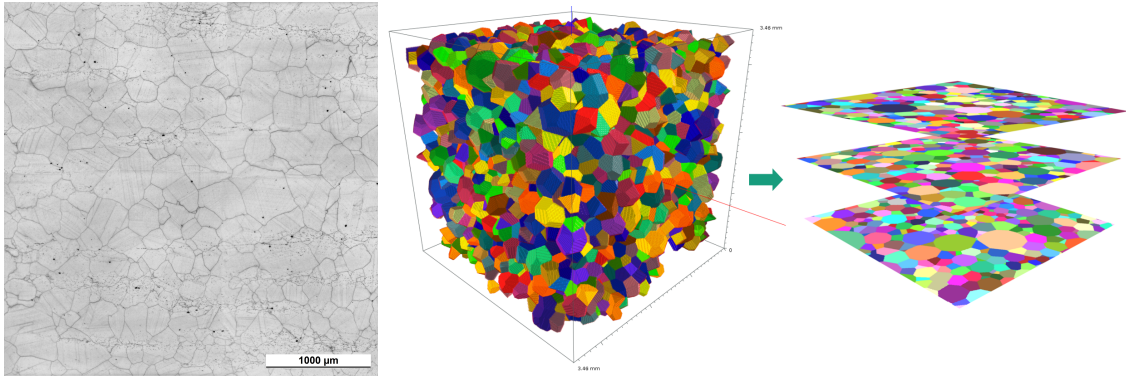


**Figure 1:** Left: Micrograph of an Inconel-617 alloy featuring the 2D parameters of the granular microstructure. Center: Visualization of a realization of the Laguerre-tessellation resulting from 4000 densely packed spheres with a log-normally distributed volume size. Right: Extracted sectional planes for comparison with the 2D micrographs.

### References

- [1] Okazaki, K. and Conrad, H. (1972). Grain size distribution in recrystallized alpha-titanium. *Transactions of the Japan Institute of Metals*, 13(3):198-204.
- [2] Fan, Z., Wu, Y., Zhao, X., and Lu, Y. (2004). Simulation of polycrystalline structure with voronoi diagram in laguerre geometry based on random closed packing of spheres. *Computational Materials Science*, 29(3):301-308.

Karl-Anton Dorph-Petersen (Aarhus University; University of Pittsburgh)

### *The History of the Cavalieri Estimator – Post, Present, and Future*

The Cavalieri estimator is one of the most fundamental workhorses of the stereologist. The estimator is used to estimate the volume of a region of interest—such as an organ or one or more of its subcompartments (e.g. the grey matter of the brain). As commonly known, in its basic form, the Cavalieri estimator requires that the whole region of interest is available for sampling and that the region of interest is well-defined with identifiable boundaries. The region is cut in its entirety, with a uniformly random position of the set of cuts, into equidistant parallel slices of constant thickness  $T$ . The volume  $V$  of the region of interest is then estimated as:

$$V := T \cdot \sum A_i$$

where the sum is across the individual areas  $A_i$  of the region of interest as observed at the cut surfaces of the individual slices. The areas may be assessed in various ways, e.g. estimated by point counting. The estimator is unbiased. I.e., by repetition, the mean of the re-estimates converges on the true mean.

The basic geometric concepts behind the estimator have been known for millennia – they were familiar to Archimedes of Syracuse (c. 287–212 BC), the Chinese mathematicians Liu Hui (c. 236) and Zu Geng (480–525) as well as to Bonaventura Cavalieri (1598–1647). The stochastic part of the estimator and its finer details evolved among stereologists during the 20th century. The modern estimator was named *The Cavalieri Estimator* in honor of Cavalieri and his famous theorem known as *Cavalieri's principle*.

In the recent years, the development of methods to predict the precision of the estimator has been a hot topic in stereological research. Also, various ways to soften the requirements of the estimator has been investigated. Thus, it has been shown that (under some constraints) the estimator is still unbiased even in the case of non-equidistant, uniformly random parallel cuts.

In my presentation, I will review the past and present of the Cavalieri Estimator and point to some areas of future development.

Tatyana Eremina (MINES Saint-Étienne)

*Local Minkowski measures for random set geometrical characterization.*

*Co-authors: Johan Debayle, Frédéric Gruy and Jean-Charles Pinoli*



**Figure 1:** Two Boolean models of rectangles with different parameters, but equal (mean) global Minkowski functionals (global area, perimeter and Euler-Poincaré characteristic).

The physico-chemical behaviour of granular media often rely on the geometrical characteristics of the particles. Quantification of parameters such as granularity, porosity, tortuosity make use of the Minkowski functionals (MFs) of the whole structure. They are also known as intrinsic volumes or quermassintegrals and play an important role in the geometrical characterization of spatial structures (in  $\mathbb{R}^2$  and  $\mathbb{R}^3$  MFs coincide up to normalization with standard geometrical parameters).

Nevertheless, facing the complex spatial structure, the global functionals appear to be not discriminating enough. For example, the simulated images in Figure 1 present the same global area, perimeter and Euler-Poincaré characteristic. Searching for a finer geometrical characterization of the structure, one could consider the local extension of the MFs - the Minkowski measures (MMs). In the present study, these local measures are considered in the Stochastic Geometry framework, i.e. applied to the random closed sets, with the object to determine their behaviour for different typical random spatial structures. The MMs distributions for the simulated germ-grain model are numerically studied.

For a given random closed set  $\Xi$  in the extended convex ring of  $\mathbb{R}^d$ , those are  $d + 1$  (random) measures on  $\mathbb{R}^d$ . Particular cases in  $\mathbb{R}^2$  are the *area measure*  $V_2(\Xi \cap \cdot)$ , *perimeter measure*  $V_1(\partial\Xi \cap \cdot)$  and Euler-Poincaré measure  $V_0(\Xi \cap \cdot)$ . In general, for  $i < d$  the measures are concentrated on the surface  $\partial\Xi$ .

The means of local MMs  $V_i(\Xi \cap B)$  in the case of statistical homogeneity are given by the product of the  $d$ -dimensional volume of  $B$  and the constant dependent on  $\Xi$  (in  $\mathbb{R}^2$  area fraction, perimeter fraction and specific Euler-Poincaré number). Thus, even for a Boolean model of disks, the expectation of local measures giving the first information about  $\Xi$  (more precisely, one could derive certain moments of the radius distribution), in general, do not determine the whole distribution. For a bit more complex structure, for example, a Boolean model with rectangular grains as in Figure 1, the individual particle geometry could not be accessed using the global MFs, neither by first moments of local MMs. In order to complete the geometrical characterization, the distributions of MMs  $V_i(\Xi \cap B)$  for the Boolean model  $\Xi$  are analysed for a special case for the random set  $B$ .

A random point uniformly distributed in  $\Xi$  determine a “center” of a closed set  $B$  (e.g. a center if  $B$  is a disk or a centroid of an arbitrary set). Thus only the spatial position of  $B$  changes. In Figure 2 for every realisation of a random point uniformly distributed in  $\Xi$ , the perimeter of intersection of the boundary  $\partial\Xi$  and a disk of radius  $r$  centred on  $x$  is computed. The correlation between the perimeter measure and particle elongation is evidenced by comparing the distributions for the Boolean models of rectangles with identical characteristics except for elongation ratio.

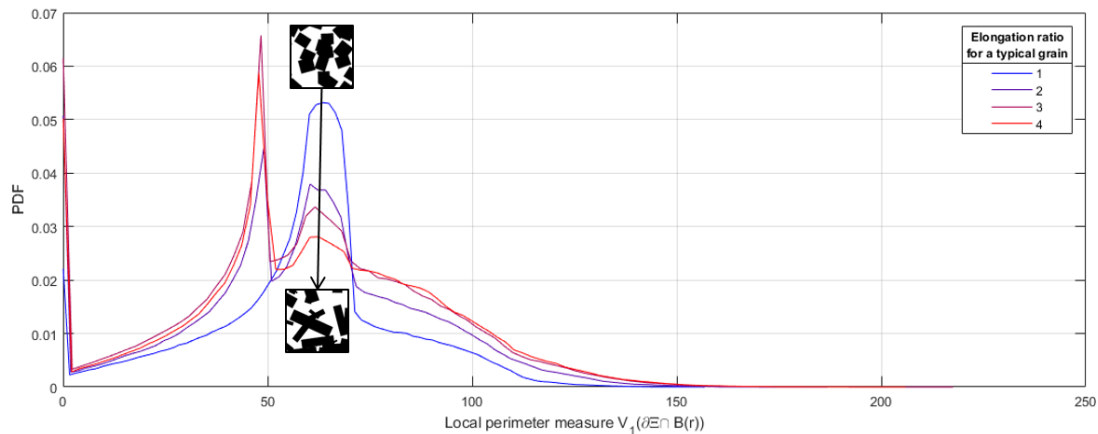


**Figure 2:** Probability density functions for the local perimeter measure of four Boolean models with rectangular grains of growing elongation ratio.  $B$  could fully lie in  $\Xi$  which leads to a peak at 0. The peak at  $2 \cdot r$  corresponds to the ball centres over the boundary  $\partial\Xi$ . Here  $r = 25$ , mean grain length varies in  $\{50, 33, 25, 20\}$ .

Next steps are the identification (if any) of the relationship of MMs distributions with the quantitative descriptors used in material science (porosity, rugosity, tortuosity, etc.). In the future, the local MMs would be studied for more complex stochastic germ-grain models than the Boolean model.

Bruno Figliuzzi (MINES ParisTech)

### *Eikonal-based models of random tessellations*

In this presentation, we describe a novel, efficient method for computing a random tessellation from its level sets representation at each voxel of a discretized domain. This method solves the Eikonal equation to compute the voxelization, which yields a complexity in  $O(N \log N)$ , where  $N$  corresponds to the number of voxels of the discretized domain. By contrast, evaluating the implicit functions of the level set representation at each voxel location results in a complexity in  $O(N^2)$  in the most general case. The method also offers the possibility to generate generalizations of the classical Voronoi or Johnson-Mehl tessellations models exhibiting rough interfaces between cells by simulating the growth of the germs on a domain where the velocity varies locally, as displayed in Figure 1 below.

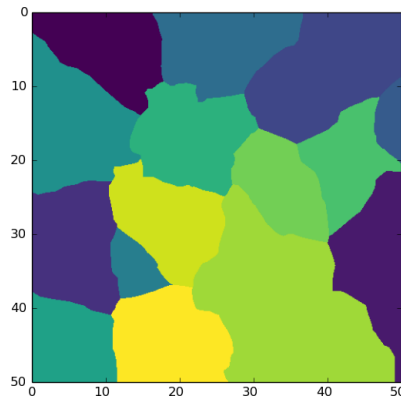


**Figure 1:** Simulation of a Voronoi tessellation with rough cells on a  $50 \times 50$  domain.

A final contribution is the development of an algorithm for estimating the multi-scale tortuosity of the boundaries of the tessellation cells. Using convex optimization tools, the algorithm computes the tortuosity of the boundary at several scales by iteratively deforming the boundary until it becomes a straight line. Using this algorithm, we show that it is possible to relate the local velocity model to the roughness amplitude observed at the cells boundaries.

Orkun Furat (Ulm University)

***Extraction of poorly visible grain boundaries from tomographic image data, using convolutional neural networks***

*Joint with Mingyan Wang, Matthias Neumann, Lukas Petrich, Matthias Weber, Carl E Krill III and Volker Schmidt*

The investigation of the morphology of grain boundaries in polycrystalline materials is of interest in the field of materials science. Sophisticated measurement techniques, like 3D X-ray diffraction (3DXRD), can determine crystallographic orientations of grains and thus provide the location of grain boundaries. However, such methods are expensive, time consuming and difficult to perform in situ, e.g., during thermodynamic treatment. More available techniques, such as X-ray microtomography, often provide challenging data when imaging alloys, since grain boundaries do not induce contrast in computed tomography (CT) image data. This work deals with image data of an aluminum-copper specimen in which a liquid attaches to grain boundaries during Ostwald ripening. Since the contrast between grain interior and boundaries can be poor in CT data for low amounts of liquid, it is difficult to extract the grain boundaries from CT data with conventional image processing techniques. Therefore, a convolutional neural network was trained with matching pairs of CT and 3DXRD data to detect poorly visible grain boundaries solely from CT data. The network's output was then segmented into grains with conventional image processing techniques like the watershed transform. This approach leads to a sufficiently good segmentation of

grains in CT data such that quantitative analysis and stochastic modeling of the grain microstructure are possible.

M. García-Amado (Universidad Autónoma de Madrid)

***A Stereological Study of the Dopaminergic Innervation and its Targets in the Human Amygdaloid complex***

*Joint with L. Prensa*

The amygdaloid complex (AC) is associated with the perception of fear and consequent anxiety related behaviors. Each AC nuclear group has particular internal and external networks and encodes different aspects of fear. Dopamine exerts its action either directly over the AC pyramidal projection neurons or by modulating the nonpyramidal interneurons (IN) which, in turn, modulate the output neurons. The activity of parvalbumin (PV) and calretinin (CR) positive (+) GABAergic IN populations is strongly affected by dopaminergic (DA) inputs. To elucidate the mechanisms of DA modulation in humans we investigate the DA innervation and its relation with the neuronal types in all AC territory. For that purpose the following studies were performed in every AC nuclear groups, nuclei and nuclear subdivisions: (1) stereological quantification of absolute number (using the optical fractionator) and density of neurons and glia; (2) stereological estimation of absolute number (using the optical fractionator) and density of the PV+ and CR+ IN, calculating the proportion of these IN with respect to the total neurons; (3) stereological quantification of the dopamine transporter (DAT)+ axon absolute length and density (using the isotropic virtual planes), and ratio between length of axon and neuron number; (4) confocal microscopy analysis of contacts between DAT+ axons and PV+ and CR+ IN. There is selective DAT+ innervation in the human AC, being in the central nucleus (main output station) twofold greater than in the basolateral group (main entrance structure). The distribution of CR+ and PV+ IN is heterogeneous and the percentage of CR+ IN with respect to the total neurons outnumbered that of the PV+ IN (13.30% for CR and 0.26% for PV; mean AC). Contacts between DAT+ axons and PV+ or CR+ IN were scant, suggesting that neither of the two IN populations is their main target. Determining the distribution, quantities, and postsynaptic targets of the DA terminals is needed to understand dopamine neuromodulation in the AC.

Supported by Fundación Eugenio Rodríguez Pascual; BFU2010-19695 and scholarship FPI-UAM.

Roman Grothausmann

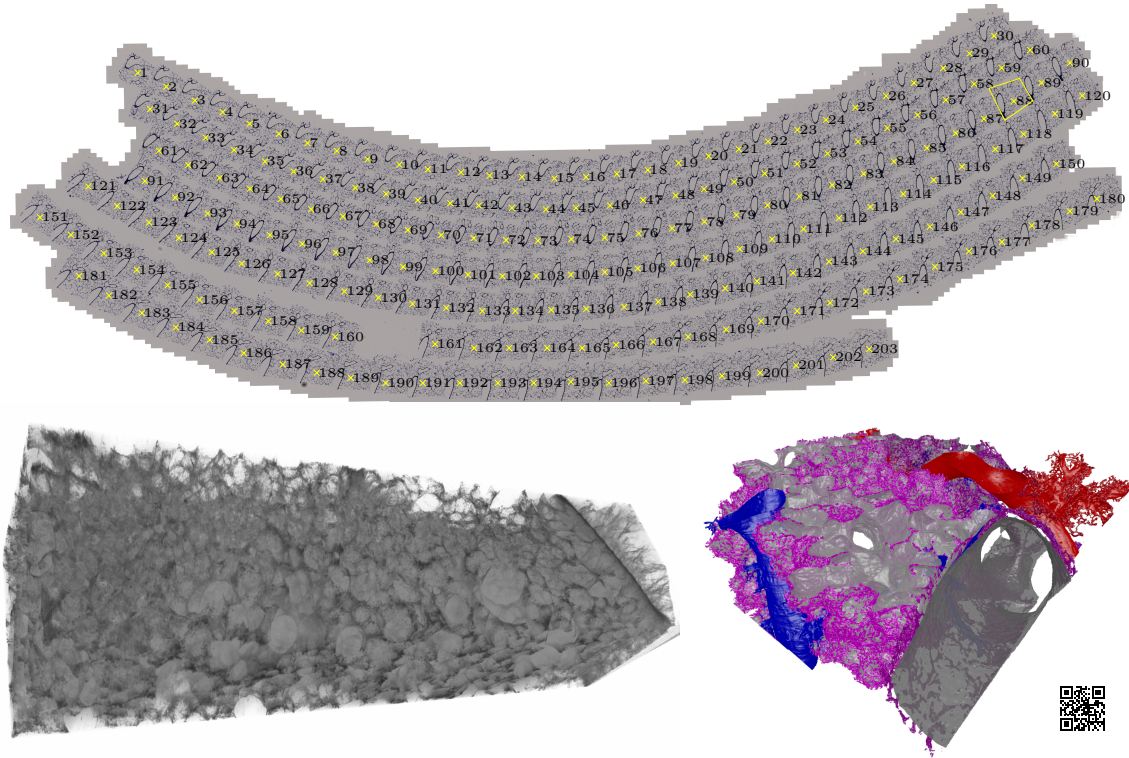
*Investigating the lung with 3D images from light and electron microscopy*

*Joint with Lars Knudsen, Matthias Ochs and Christian Mühlfeld*

The closer the look, the more complex are the structures of the lung and the more challenging become their analyses. New insights into the astonishing architecture and the complicated developmental dependencies are gained by pairing 3D imaging techniques based on light and electron microscopy. However, the resulting 3D images are very large (ranging from a few Gigabytes to a few Terabytes) and not easy to grasp neither visually nor analytically. Even though stereology can be employed to quantify aspects of these datasets, some questions can only be answered with 3D digital image processing. This often demands segmenting the structures of interest, like tissue, airspaces and blood vessels.

Manual segmentations are often regarded as the most reliable but are also most tedious and time-consuming to create. Methods exist that segment the data fully automated such as conventional image filters (e.g. watershed, level-sets, graph cuts) or machine learning (in particular Deep Learning, e.g. 3D U-Net, DeepMedic). However, fully automated segmentations without any manual intervention often yield results that do not represent the underlying anatomical structures sufficiently exact. It is possible to combine automation with manual interaction when segmenting the data. The automatic methods are chosen to produce multiple partial 3D segments that are then assigned manually to each structure of interest. This procedure can be a good trade-off between speed and exactness, ensuring that the final segmentation was thoroughly inspected visually.

These segmentations then not only enable to quantify simple measures like volume and surface area of the structures of interest but also diffusion distances, regions of supply and topological characterizations of the alveolar capillary network. Additionally, the segmentations allow sophisticated visualizations along extracted paths either for virtual endoscopy or for straightening the data.



Tom Dela Haije (University of Copenhagen)

***Imaging Brain Fibers with Diffusion MRI***

Diffusion-weighted magnetic resonance imaging (MRI) can be used to image the aggregate microscopic motion of water molecules in living tissue. By exploiting correlations between the main directions of this motion and the orientations of fibrous structures such as nerve fibers in the human brain, we can reconstruct approximate maps of the global connections between different brain regions. In this presentation I will give a brief introduction of diffusion-weighted MRI, the different structural properties that this technique is sensitive to, some of the current challenges faced by this field, and the potential added value of for example fiber processes in the resolution of these challenges.

Konstantin Hauch (TU Kaiserslautern)

***Stochastic Modeling of Fiber-reinforced Ultra High Performance Concrete based on 3D Image Analysis***

*Joint with Kasem Maryamh, Claudia Redenbach and Jürgen Schnell*

Desirable properties of concrete in buildings are high compressive and tensile strength and load-bearing capacities. Ultra High Performance Concrete (UHPC)

is characterized by a high compressive strength. The load-bearing capacity and the tensile strength can be increased by adding steel fibers to the concrete. The orientations and the positions of the fibers in the concrete considerably determine its properties. For instance, the load-bearing capacity is maximal if the direction of the loading force is perpendicular to the fiber orientation. A homogeneous distribution of the fibers in the concrete leads to a homogeneous load-bearing capacity.

The orientations and positions of the steel fibers depend on many parameters in the production process. Length, diameter and volume fraction of the fibers, the amount of superplasticizer, the pouring direction, and the formwork for the concrete are just a few examples of these parameters. To investigate these dependencies, a large number of samples of fiber-reinforced UHPC with varying parameters was produced. The samples were imaged by using micro computed tomography ( $\mu$ CT) and the fiber system was reconstructed by a suitable segmentation algorithm.

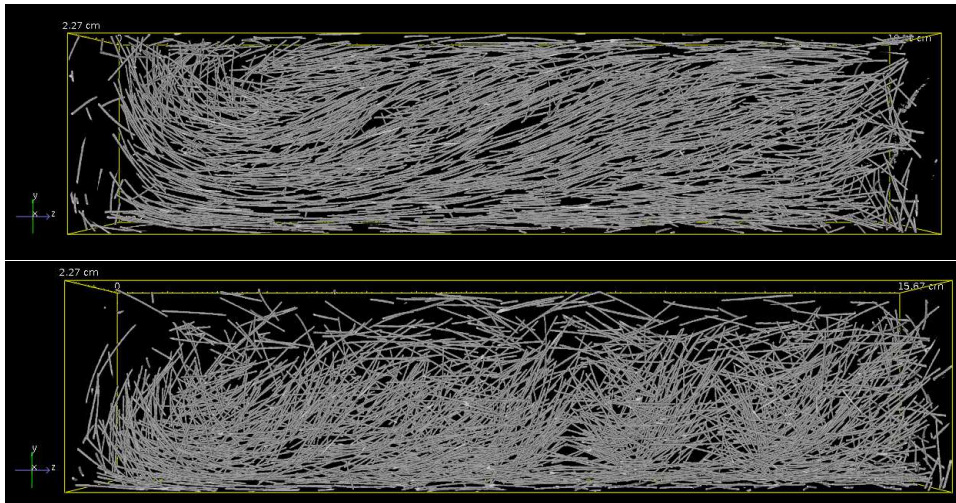


**Figure 1:** Visualisations of reconstructed tomographic images of a steel fiber-reinforced UHPC. The steel fibers in both samples have a diameter of 0.3 mm and a length of 12 mm. The volume fraction of fibers in the UHPC is 1%. In the sample in the bottom 20% more superplasticizer was used.

Statistical analysis showed that the fiber diameter and the amount of superplasticizer have an effect on the orientations and the spatial distribution of the fibers (see Figure 1). Furthermore, the orientation of the fibers changes depending on their position in the UHPC. In bending tests, the load-bearing capacity of the fiber-reinforced UHCP is measured. CT imaging additionally allows for an investigation of correlation between crack locations and the local fiber geometry. Finally, a method for predicting the mechanical properties of the fiber-reinforced UHPC using a stochastic model is outlined.

Kateřina Helisov (Czech Technical University in Prague)

***Similarity of realisations of random sets via approximation by unions of convex compact sets***

*Joint with Vesna Gotovac and Ivo Ugrina*

The talk concerns a similarity measure of realisations of random sets through a heuristic based on approximation by unions of convex compact sets, evaluation of the support functions of the approximating sets and consequent usage of envelope tests and  $N$ -distances. The measure is used to distinguish between two realisations, more precisely to decide whether two given realisations come from the same underlying process when we have their pixel images. The suggested procedure is justified through simulation studies of common random models like Boolean model and Quermass-interaction processes with different parameters.

C. Vyvyan Howard (University of Ulster)

***The detection of subtle changes in 3D microstructural relations in the CNS using 2nd order stereological methods measured with isotropic linear rulers.***

*Joint with Gesa Staats and Matthew Reed*

The use of isotropic linear probes to elicit 2nd order stereological estimates offers a number of advantages. As the result of a conscious effort to combine the benefits of rigorous unbiased stereological techniques with the simplest possible experimental implementation we developed the One Stop Stereology technique. Measurements can be made on thin sections with IUR or VUR sampling properties. Thus the approach can be applied to historical collections of histological material. The fact that most laboratories using stereological methods tend to sample and subsequently store material in blocks of VUR sampled tissues makes the approach potentially widely applicable. The technical aspects of the application of isotropic linear rulers has been described ([6]). The approach has been dubbed ‘One-stop stereology’ (OSS) because, at one sitting it is possible to measure: (i) the volume fraction,  $V_V(A_i, ref)$ , for each phase from the Rosiwal ([7]) relationship  $L_L = V_V$ . (ii) the surface density for each phase,  $S_V(A_i, ref)$ , from the classical relation  $S_V = 2I_L$  (e.g. [10]), (iii) the volume weighted star volume of each phase, which is equal to the volume weighted mean particle volume for a phase consisting of discrete particles, using the methods of [5, 9, 3], (iv) the contiguity and matrix of surface affinities between all pairs of phases ([4]), (v) if VUR sections are used, the ‘volume anisotropy’ using star-volumes (e.g. [2]), (vi) the volumetric set covariance,  $C(h, A_i)$  for each phase, i.e. the probability that a pair of points separated by a distance  $h$  units will simultaneously hit phase  $A_i$ . (vii) all crosscovariance functions,  $C(h, A_i, A_j)$ , for each pair of phases ( $i \neq j$ ), i.e. the probability that a pair of points separated by a distance  $h$  units will hit phases  $A_i$  and  $A_j$ , (viii) the ‘star’ covariance for each phase,  $C^*(h, A_i)$ , i.e. the probability that a pair of points separated by a

distance  $h$  units will both hit phase  $A_i$  and be joined by a straight line fully within the phase ([1]), (ix) a range of linear contact distribution functions ([8]).

This paper will describe the application of OSS to the study of the effect of fetal exposure to the NMDA antagonist MK801 on the postnatal development of rat brain. Subtle changes to the spatial relationship between glial and neuronal cells in the subiculum were demonstrated through the measurement of crosscovariance. No differences between experimental and control groups were found with 1st order estimators.

### *References*

- [1] Cabo, A.J. & Baddeley, A.J. (1994) Estimation of mean particle volume using the set covariance function. Research Report 1994/14, Department of Mathematics, The University of Western Australia.
- [2] Cruz-Orive, L.M., Karlsson, L.M., Larsen, S.E. & Wainstein, F. (1992). Characterising anisotropy: A new concept. *Microscopica Acta*, 23 75–76.
- [3] Gundersen, H.J.G. & Jensen, E.B. (1985). Stereological estimation of the volume-weighted mean volume of arbitrary particles observed on random sections. *J. Microsc.* 138, 127–142.
- [4] Kroustrup, J.P., Gundersen, H.J.G and Vaeth, M. (1988) Stereological analysis of 3-dimensional structure organisation in multiphase specimens – statistical-methods and model-inferences. *J. Microsc.* 149, 135–152.
- [5] Miles R.E. (1977) The importance of proper model specification in stereology. Geometrical probability and biological structures, Buffon's 200th anniversary. Proceedings, Paris 1977. (ed by R.E. Miles and J. Serra), pp 115–136. Lecture notes in Biomathematics. No 23. Springer-Verlag, Berlin.
- [6] Reed MG, Howard CV & Staats de Yanes G (2010). One-Stop Stereology: the estimation of 3D parameters using Isotropic Rulers. *Journal of Microscopy*, 239: 54–65.
- [7] Rosiwal, A. (1898). Über geometrische Gesteinsanalysen. *Verh. K. K. Geol. Reichsanst., Wien*, 13, 143–175.
- [8] Saxl, I. (1993) Contact distances and random free paths. *J. Microsc.* 170, 53–64
- [9] Serra, J. (1982). *Image Analysis and Mathematical Morphology*. Academic Press, London.
- [10] Smith, C.S. & Guttman, L. (1953). Measurement of internal boundaries in three-dimensional structures by random sectioning. *Trans. AIME*. 197, 81.

Lucie Kubínová (Czech Academy of Sciences)

***Possibilities of virtual reality approach for measurement and 3D visualization of tubular microstructures***

*Joint with Jiří Janáček, Antonín Požusta, Diana Siswantonová, Xiao Wen Mao, Anastasiya Klebanovych and Pavel Dráber*

3D visualization and measurement of structural characteristics of different types of tubular microstructures are of interest in many biological studies – visualization is important for qualitative examination and formulation of hypotheses on structural changes under different conditions, while quantitative measurements can be used for testing the hypotheses. However, it can be difficult for the observer to perceive the exact organization of complex structures rendered 3D and measurements of structural characteristics by stereological and other interactive methods are often tedious and time-consuming. In our study, we tested possibilities of virtual reality (VR) as a tool that could enhance exploration and interaction within 3D microscopic images of tubular structures. We developed a custom-made VR image analysis software, capable of rendering a very high resolution VR image of microstructures to high-end enterprise head mounted display (developed by VRgineers). Goggles were tracked using absolute position tracking system developed by DTrack. The application rendered images to the virtual space around the user, enabling him/her to move and interact using his/her own hands or specialized controllers with rendered 3D reconstruction of acquired microscopic images. Acquired microscopic images of microstructures were converted into a volumetric object, which was then rendered to each eye using ray casting technique. User was able to walk through the rendered structure and to mark up, draw and thus measure parts of the tissue. Application was developed in .Net framework and DirectX 11 considering optimized algorithms for fluent visual perception. We tested VR approach on two types of tubular structures, acquired by confocal or STED microscopy techniques:

1. Microtubules (MT), i.e. cylindrical cytoskeletal polymers indispensable for many vital cellular activities, representing a dense and complex network of fibers inside cells. The individual fibers could be poorly separated, due to low resolution of microscopic images. Virtual reality approach enabled to enhance perception of organization of MT in human osteosarcoma cell U2OS acquired by STED microscopy.
2. Blood capillaries, important tubular structures, supplying living tissues with nutrients and oxygen while simultaneously removing metabolic waste products. Capillaries, acquired by confocal microscopy, represent a complex net of well-separated tubes. Virtual reality approach was applied for clear visualization, as well as for capillary length measurement. The results of measurement of the length of rat brain capillaries obtained by VR approach were in accordance with results obtained by more tedious approaches ([1]) using stereological methods based on a computer generation of isotropic

uniform random virtual test probes in 3D, or interactive “tracer” method based on a manual delineation in 3D stacks of images.

This work was supported by the Grant Agency of the Czech Republic (17-11898S), MEYS (LM2015062 Czech-BioImaging and CZ.02.1.01/0.0/0.0/16\_013/0001775 funded by OP RDE).

#### *References*

- [1] Kubínová L, Mao XW, Janáček J: Blood capillary length estimation from three-dimensional microscopic data by image analysis and stereology. *Microscopy and Microanalysis* 19: 898–906, 2013.

Arvydas Laurinavičius (Vilnius University Hospital)

#### ***The Benefits of Digital Pathology***

Digital pathology comes with countless opportunities for innovation in pathology services. One major direction of the progress relies on a multitude of methods and their combinations to retrieve new quality of information by tissue-based testing. Digital imaging techniques, image analysis and analytics lead beyond conventional pathology testing with augmented vision and intelligence transforming it into deep context pathology assays. Taking into account spatial heterogeneity and tissue microenvironment aspects, along with retrieval of sub-visual indicators of the disease, the assays will enable new level of informative power for precision medicine. Another aspect of the progress relates to pathology workflow integration within the laboratory and into clinical environment. Pathology information systems maintain their crucial role in this process; however, they need to transform into highly flexible and intelligent systems to improve workload management, lean processes, human-machine interaction efficiencies, expertise sharing, decision-support, patient and sample-centric communication of pathology and multidisciplinary teams. Pathology is inevitably moving online to provide service in “no space and time”.

David Legland (INRA)

#### ***Orientation maps from gray-level images using oriented granulometry***

*Joint with Alain Bourmaud and Victor Gager*

Natural fibres are now widely used as reinforcements for semi-structural and structural composite applications. The mechanical properties of the resulting composites highly depend on the morphology and on the organisation of the fibres, in particular their orientation. A first approach to describe morphology of composite fibres is to segment each fibre individually and quantifying its morphology, resulting in a distribution of morphometric features such as length

or thickness values. However, the imaging of large collections of fibres makes their identification often problematic.

Texture analysis is an alternative to object-based analysis that allows describing local variations of gray levels. We propose a novel method based on gray level granulometry by mathematical morphology that allows describing preferred orientation of fibres from gray level images [1,2]. We use a family of linear structuring elements with variable size and orientation that allows applying morphological opening and closing of increasing sizes. Granulometric curves and gray level mean sizes can be computed for each orientation around pixel of the image. An estimate of the preferred orientation for each pixel is computed, that allows to build an orientation map from the input image, and to generate a histogram of orientations.

The methodology was applied to electron microscopy images of fibres (synthetic and natural) used for composite reinforcement. Orientation histogram computed on images of glass fibre unidirectional preform validates the method. Similar analyses performed on images of a flax nonwoven could reveal a preferred orientation of fibres that could be related to the manufacturing process. This new method raises interesting perspectives for determination of fibres and bundles diameters, estimation of the orientation in the three dimensions or finally numerical modelling of biocomposite properties.

#### *References*

- [1] P. Soille, *Morphological Image Analysis*. Springer, 2003.
- [2] M. F. Devaux, B. Bouchet, D. Legland, F. Guillon, and M. Lahaye, "Macro-vision and grey level granulometry for quantification of tomato pericarp structure," *Postharvest-Biol. Technol.*, vol. 47, no. 2, pp. 199–209, 2008.

Rory E. Morty (Max Planck Institute for Heart and Lung Research)

#### ***Estimation of absolute number of alveolar epithelial type 2 cells in mouse lungs: a comparison between stereology and flow cytometry***

Accurate estimation of the absolute number of a particular cell-type in whole organs is increasingly important in studies on organogenesis, and the remodelling and repair of diseased tissues. The unbiased estimation of the absolute number of cells in an organ is complicated, and design-based stereology remains the method of choice. This has led investigators to explore alternative approaches – such as flow cytometry – as a faster and less labour-intensive replacement for stereology. To address whether flow cytometry might substitute stereology, design-based stereology was compared with microfluorosphere-controlled flow cytometry, for estimation of the absolute number of alveolar epithelial type 2 cells (AEC2) in the lungs of two mouse strains: wild-type C57BL/6J mice and *Sftpc*-YFP mice. Using design-based stereology,  $\approx 10.7$  million and  $\approx 9.0$  million AEC2 were estimated in the lungs of wild-type C57BL/6J mice and *Sftpc*-YFP mice, respectively. Substantially fewer AEC2 were estimated using flow cytometry.

In wild-type C57/BL6J mouse lungs, 59% of the AEC2 estimated by design-based stereology were estimated by flow cytometry ( $\approx 6.3$  million), using intracellular staining for pro-surfactant protein C. Similarly, in *Sftpc*-YFP mouse lungs, 23% of the AEC2 estimated by design-based stereology were estimated by flow cytometry ( $\approx 2.1$  million), using yellow fluorescent protein fluorescence. Our data suggest that flow cytometry underestimates AEC2 number, possibly due to impaired recoverability of AEC2 from dissociated lung tissue. These data suggest design-based stereology as the method of choice for the unbiased estimation of the absolute number of cells in an organ.

Mads Nielsen (University of Copenhagen)

***Deep learning in pathology***

By digitalisation of pathology, not just storing, viewing, and indexing may be automated. Also, the visual inspection may be partly handled by a computer.

Recent development in deep learning powered by the applications in computer vision using the convolutional neural networks has given the accuracy and precision of automated image analyse a quantum leap. Earlier approaches included handcrafted features and adapted pattern recognition algorithms. Nowadays indexical computational structures are used for many different application. Especially the U-net has shown an amazing performance and rebustness in medical image analysis.

We will discuss the trends in deep learning in medical image analysis, show examples of implementations, discuss the applications in pathology, and discuss the technical tricks necessary for making the applications work in practice.

Matthias Ochs (Charité – Universitaetsmedizin Berlin; German Center for Lung Research)

***State of the art EM techniques for quantitative assessment of lung structure***

In order to understand how the mammalian lung functions as a gas exchanger, one has to do two things: looking inside the lung and measuring its structure. Both aspects require adaequate methodology. Regarding the first aspect, the cellular details of the barrier separating air and blood can only be resolved by electron microscopy. Regarding the second aspect, the gold standard for obtaining quantitative (morphometric) data on lung structure in microscopy is stereology. This research field was pioneered by Ewald Weibel (1929–2019). Meanwhile, stereology as the method of choice for quantitative assessment of lung structure is endorsed by an official research policy statement of the American Thoracic Society and the European Respiratory Society (Hsia, Hyde, Ochs, Weibel: *Am J Respir Crit Care Med* 2010;181:394–418).

A new dimension to electron microscopy of the lung was added by 3D techniques. They comprise a broad spectrum of recent developments and advances in

instrumentation and specimen preparation and include serial block face scanning electron microscopy (SBF-SEM), focused ion beam scanning electron microscopy (FIB-SEM), and electron tomography (ET). These methods are complementary regarding sample size and resolution. They provide 3D datasets of the lung much more efficiently and at higher quality than conventional serial section transmission electron microscopy (Ochs, Knudsen, Hegermann, Wrede, Grothausmann, Mühlfeld: *Histochem Cell Biol* 2016;146:695–707).

In this presentation, I will review the history of lung microscopy and stereology, and provide an overview on current 3D EM techniques, their application to the study of lung micro-structure, and their potential for stereological studies.

D.E. Oorschot (University of Otago)

***Changes in midbrain dopaminergic circuitry in the maternal immune activation rat model of schizophrenia: ultrastructural stereological analyses***

*Joint with L.C. Parr-Brownlie, R. Smither, H. Wicky, S.M. Hughes, D.K. Bilkey and S. Seo*

Schizophrenia is a debilitating neuropsychiatric disorder with ~1% prevalence. Despite extensive research, little is known about the microscopic changes in neural circuits that may contribute to the behavioural manifestations of schizophrenia. We have identified a complex pattern of inputs onto the dopaminergic neurons in the posterior ventral tegmental area (pVTA) of the midbrain, involving inhibitory inputs from the rostromedial tegmental nucleus (RMTg), which in turn are modulated by excitatory glutamatergic inputs. Here, we investigated the hypothesis that an underlying causal mechanism of schizophrenia is altered synaptic input onto pVTA dopaminergic neurons, which results in a characteristic excessive release of dopamine. We combined lentiviral vector technology and peroxidase-immunogold double labelling methods to selectively label pVTA dopaminergic neurons and RMTg GABAergic neurons. Three-dimensional serial transmission electron microscopy was used to analyze the synaptic inputs to the pVTA in the maternal immune activation (MIA) rat model of schizophrenia versus controls. In identified synapses between RMTg GABAergic neurons and pVTA dopaminergic neurons, we found a statistically significant decrease in the volume of both the presynaptic terminal and the postsynaptic density in MIA rats versus controls. For excitatory synapses on the RMTg GABAergic inputs, we found a statistically significant decrease in the thickness of the postsynaptic density in MIA rats versus controls. All anatomical deficits correlated significantly with decreased pre-pulse inhibition. These data suggest that in schizophrenia, impaired inhibition of pVTA dopaminergic neurons could result in excessive release of dopamine, leading to a hyperdopaminergic state of the brain and the manifestation of schizophrenic symptoms.

Johannes A. Österreicher (Austrian Institute of Technology)

***Information depth in backscattered scanning electron microscopy***

*Joint with Florian Grabner, Andreas Schiffl, Sabine Schwarz, Gilles R. Bourret*

In many fields of science and technology, the quantification of nanoparticles dispersed in a solid matrix is an important task. This is often accomplished by transmission electron microscopy (TEM) which is expensive and laborious. Scanning electron microscopy (SEM) is far more affordable, offers easier sample preparation, and a larger analytical area. However, the information depth in backscattered SEM is usually unknown as it depends on acceleration voltage, chemical composition of matrix and particles, as well as the size of the embedded particles. When the information depth is unknown, volumic number densities and unskewed size distributions cannot be obtained.

Here we present a stereological technique for the quantification of nanoparticles by backscattered SEM that takes size and composition of sub-surface particles into account and assigns information depth accordingly. The resultant function of information depth over particle size allows for the reconstruction of the size distribution and number density. The method is based on Monte Carlo simulations of the interaction of electrons with solids containing particles and analysis of the signal-to-noise ratio. Application of the method to experimental backscattered electron micrographs and validation by TEM showed very good agreement for dispersoids in an Al alloy while using previous estimates of information depth resulted in large deviations.

The method is computationally very efficient, uses only cost-free software, and can be easily adapted to other material combinations in many fields of research. It is entirely physically based and does not require any fitting parameters.

Zbyněk Pawlas (Charles University)

***Limit theorems for random marked tessellations***

By a marked particle process we understand a simple point process in  $\mathcal{K}' \times \mathbb{M}$ , where  $\mathcal{K}'$  denotes the space of non-empty compact subsets of  $\mathbb{R}^d$  and  $\mathbb{M}$  denotes the mark space. A random marked tessellation is then a special case where the corresponding unmarked particle process is a random tessellation in  $\mathbb{R}^d$ . For stationary random marked tessellations the intensity describes the mean number of cells per unit volume and the grain-mark distribution describes the joint distribution of a typical cell and its corresponding mark. We consider the estimators of these first-order characteristics and investigate their asymptotic behaviour as the observation window is expanding. For several particular models we are mainly interested in weak or strong consistency, variance asymptotics and asymptotic normality.

Daniel A. Peterson (Rosalind Franklin University of Medicine and Science)

***Assessing in vivo neuronal reprogramming by automated, resonance-scanned confocal virtual tissue image acquisition and artificial intelligence-assisted stereology***

*Joint with Mentor Thaqi*

Direct in vivo reprogramming of non-neuronal cells in the mature CNS into phenotypically correct neurons can be achieved through forced expression of pioneering transcription factors, such as Ngn2, NeuroD1, and Ascl1, that normally act to direct neuronal fate specification during development. This process produces a variable population of induced neurons that can be identified through their expression of reporter genes tied to the induction process and expression of various neuronal phenotypic markers, requiring detection of multiple fluorescence labels with resolution by confocal microscopy. Following in vivo gene delivery of lineage instruction factors, the number of infected cells and their distribution present some challenges for accurate quantitation by design-based stereological sampling. Generally, too many cells are infected to completely count with accuracy across histological sections arguing for subsampling of the population by stereological principles. In addition, cell density varies widely from the site of injection to the most distant infected cells. This means that sampling frequency density must be high to reduce estimator variance to an acceptable level. Furthermore, traditional acquisition of confocal stacks is time consuming and inefficient. The recent availability of resonance scanning confocal microscopes permits the rapid generation of virtual section data sets. Efficient sampling design can now follow complete image acquisition of the histological material. The application of artificial intelligence to detecting cells with different label combinations within the virtual section data set makes it possible to automate cell counting if detection criteria can be achieved. However, cell detection must be combined with stereological sampling principles to account for sectioning and other artifacts and to accommodate fractionated sampling. These approaches are appropriate for other “rare” cell populations, such as grafted cells, and could be extended to dense cell populations if shown to be efficient.

Supported by US National Institutes of Health NS 100514.

Lukas Petrich (Ulm University)

***Recognition of meadow saffron sites in drone images, using a machine-learning approach***

*Joint with Georg Lohrmann, Matthias Neumann, Fabio Martin, Andreas Frey, Albert Stoll and Volker Schmidt*

Meadow saffrons (*Colchicum autumnale*) are toxic autumn-blooming flowering plants, which often grow on meadows and pastures, and thus pose a threat to farm animals especially in hay. However, weed control is often difficult on these grounds since it is desired to minimize the damage to the fauna and surrounding flora. That is why site-specific counter measures, targeting only a small area around the toxic plants, are sought.

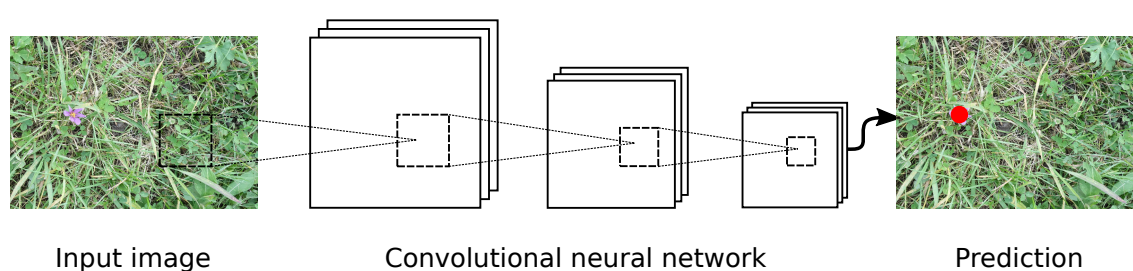


**Figure 1:** Visualization of the presented method to recognize meadow saffrons sites. (To improve visibility, no drone images are shown.)

One option is to employ drones to acquire high-resolution photos (in the visible light range) of the fields. Since the geolocation is tracked, it is then possible to locate the meadow saffrons on these images and to compute their exact GPS-position using offline methods. Based on these detected sites, application maps for the weed control tools, such as heat treatment or cutting, are created.

In this talk a procedure to localize blooming meadow saffrons in drone images is presented. This approach relies on convolutional neural networks to recognize the blossom sites, see Figure 1. The training data based on hand-labeled images is further enhanced through image augmentation, which leads to improved stability of the prediction against, e.g., alterations of lighting.

Benedikt Prifling (Ulm University)

***Stochastic 3D microstructure modeling of differently compacted cathodes in lithium-ion batteries***

*Joint work with Daniel Westhoff, Denny Schmidt, Henning Markötter, Ingo Manke, Volker Knoblauch, Volker Schmidt*

Lithium-ion batteries are one of the most promising technologies for storing electrical energy due to their preferable electrochemical properties. Thus, they are currently used in a large number of applications ranging from portable devices to

electric vehicles. It is known that the electrode morphology strongly influences the overall battery performance. Therefore, a deeper understanding of the microstructure is an important task regarding the optimization of electro-chemical performance. Thus, the investigation of the manufacturing process and its impact on the microstructure is one main task in battery research. The 3D morphology of eight differently compacted cathodes has been obtained using synchrotron tomography. With the help of image processing techniques, as for example a marker-based watershed algorithm with extended regional minima, we obtain a phase-based as well as a particle-based segmentation, see Figure 1.

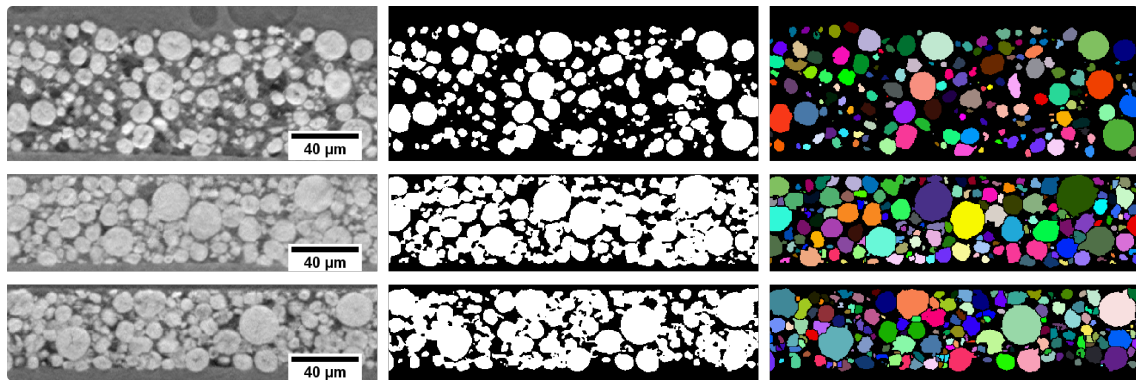


**Figure 1:** Through-plane cross sections of cathode microstructure for a compaction load of 0, 400 and 1000 MPa (from top to bottom). Left column: original 16-bit grayscale image. Middle column: Phase-based segmentation. Right column: Particle-based segmentation.

Thus, we are able to quantify the changes of the cathode morphology by means of numerous image characteristics. In addition, we are able to calibrate one and the same type of a parametric stochastic 3D microstructure model to all compaction loads. The goodness of fit is quantified by phase-based as well as particle-based image characteristics. A visual comparison between tomographic image data and a virtually generated cathode microstructure is shown in Figure 2. The utilization of a parametric model allows us to describe the complex 3D morphology of the cathode using only a few parameters. By least-squares regression analysis, we are finally able to predict the model parameters and hence the morphology of cathodes for arbitrary compaction loads. This can be used to provide a wide spectrum of virtual but realistic 3D microstructures as valuable input for numerical simulations of charge transport.

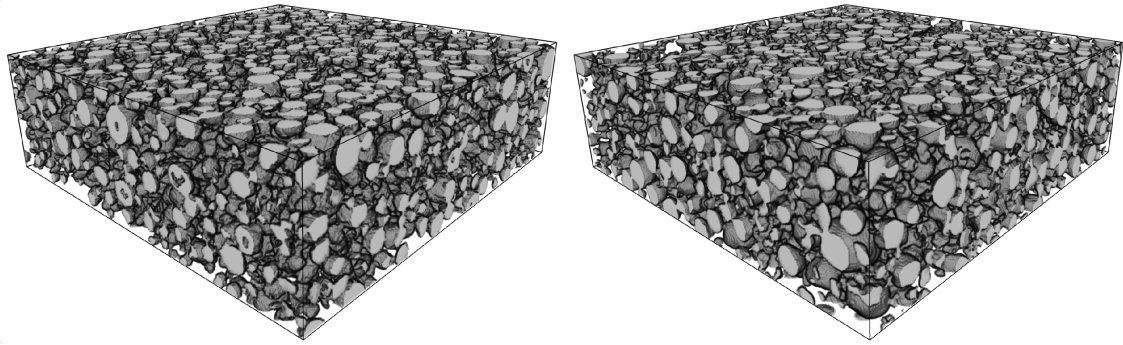


**Figure 2:** 3D rendering of tomographic image data (left) and virtually generated microstructure (right) for a compaction load of 0 MPa.

Allan Rasmusson (Vilnius University)

***Quality assurance of digital image analysis by stereological estimation using stratified sampling***

*Joint with Benoit Plaincoulaine and Arvydas Laurinavicius*

In the quest for high-capacity image analysis, for instance for screening of drug components and within the emerging field of digital pathology, companies and laboratories turn to automated, digital image analysis. In essence, it is favourable to acquire ever-more powerful computers to lower turn-around times rather than employ more personnel to perform manual or computer-assisted stereology. While high-capacity automated image analysis may provide consistent results very quickly, it remains of utmost importance to ensure that it delivers accurate and precise results, and to maintain the possibility for quick evaluation of individual outlier cases.

It has previously been suggested to change the role of, say, an expert pathologist from estimating quantities to instead evaluate the accuracy of the applied image analysis methods. If this is furthermore done by inspecting the same objective events that form the basis of stereological methods, the evaluation efforts can be lowered by employing more efficient sampling schemes. Unfortunately, the simpler sampling schemes proved to still be too time-consuming while the more efficient proportional sampling turned out to be insufficient.

We investigated quality assurance of digital image analysis based on recent works in stereological estimation using a stratified sampling approach which can be seen as a combination of simple and proportional sampling. Presented here is a proof-of-concept of efficient unbiased image analysis evaluation, including sampling scheme parameter determination and potential pitfalls in image analysis evaluation. We conclude that estimation by stratified sampling enables manual verification of automated whole slide images in a way that is easily integrated into image analysis pipelines like digital pathology workflows.

Magnus Röding (RISE Research Institutes of Sweden)

***Quantitative microscopy for characterizing material microstructures and mass transport***

To understand porous material microstructures and their mass transport properties, and ultimately to learn how to tailor materials for specific purposes, quantitative characterization using statistical models and methods is key. In this talk, we give three examples of quantitative methods in microscopy for this purpose.

First, we describe how single particle tracking (SPT) based on confocal laser scanning microscopy data can be used to estimate local diffusion coefficients, sizes, and concentrations of fluorescent nanoparticles in liquid suspension. Estimation is performed using simulation-based inference, specifically Approximate Bayesian Computation (ABC). The method is widely applicable for characterization of natural and man-made nanoparticles, including biological fluids like blood. We also demonstrate good performance on a validation case [1].

Second, we describe a new numerical model based on spectral-domain numerical methods for modeling of data from fluorescence recovery after photobleaching (FRAP) experiments. FRAP is a widely used technique for estimation of both local diffusion coefficients and binding kinetics i.e. association and disassociation rate constants, to understand heterogeneity, obstruction effects, structural dynamics, and interactions with a matrix in soft matter. This new FRAP model is one of the most comprehensive to date, and we show good agreement with previous literature on a validation case [2].

Third, we present a new method for segmentation of image data acquired using focused ion beam scanning electron microscope (FIB-SEM) nanotomography. FIB-SEM is a powerful technique for 3D imaging of nanoporous microstructures, allowing for substantially higher spatial resolution than e.g. X-ray tomography. A 3D data set is acquired in a serial fashion where in-between each image, a slice of the sample is milled away using the ion beam of the FIB to reveal a new planar cross-section, which is imaged using the SEM. The technique is challenging due to e.g. the fact that it produces a stack of 2.5D rather than 2D images, with subsurface pore information shining through. We propose a random forest classifier combined with scale-space feature extraction, yielding good agreement with manual segmentations on three data sets of porous polymer films [3].

*References*

- [1] M Röding, M Billeter. Massively parallel approximate Bayesian computation for estimating nanoparticle diffusion coefficients, sizes and concentrations using confocal laser scanning microscopy. *Journal of Microscopy*, 2018, 271, 174–182.
- [2] M Röding, L Lacroix, A Krona, T Gebäck, N Lorén. A highly accurate pixel-based FRAP model based on spectral-domain numerical methods. *Biophysical Journal*, 2019, DOI: 10.1016/j.bpj.2019.02.023.

- [3] M Röding, C Fager, A Olsson, C von Corswant, E Olsson, N Lorén. Three-dimensional reconstruction of microporous polymer films from FIB-SEM nanotomography data using random forests. Submitted to *Microscopy and Microanalysis*.

Volker Schmidt (Ulm University)

***Quantifying the influence of 3D microstructure on effective conductivity and permeability of composite and porous materials***

*Joint with Matthias Neumann, Ole Stenzel, François Willot and Lorenz Holzer*

Effective conductivity and permeability of a versatile, graph-based model of random structures are investigated numerically. This model, originally introduced in [1] allows one to simulate a wide class of realistic materials. In the present work, an extensive dataset of two-phase microstructures with wide-ranging morphological features is used to assess the relationship between microstructure and effective transport properties, which are computed using Fourier-based methods on digital images. Our main morphological descriptors are phase volume fractions, mean geodesic tortuosity, two “hydraulic radii” for characterizing the length scales of heterogeneities, and a “constrictivity” parameter that describes bottleneck effects. This additional parameter, usually not considered in homogenization theories, is an essential ingredient for predicting transport properties, as observed in [1]. We modify the formula originally developed in [2] for predicting the effective conductivity and propose a formula for permeability. For the latter one, different geometrical definitions of the hydraulic radius are compared. Our predictions are validated using tomographic image data of fuel cells.

*References*

- [1] G. Gaiselmann, M. Neumann, O. M. Pecho, T. Hocker, V. Schmidt, L. Holzer (2014): Quantitative relationships between microstructure and effective transport properties based on virtual materials testing. *AIChE Journal* 60, 1983–1999.
- [2] O. Stenzel, O. M. Pecho, L. Holzer, M. Neumann, V. Schmidt (2016): Predicting effective conductivities based on geometric microstructure characteristics. *AIChE Journal* 62, 1834–1843.

Filip Seitzl (Charles University)

***Applications of Gibbs-Laguerre tessellations to the modeling of polycrystalline materials***

*Joint with L. Petrich, C. E. Krill III, V. Schmidt, J. Staněk and V. Beneš*

In materials research, three-dimensional (3D) grain structure of polycrystalline metals is investigated. An adequate probabilistic model for the microstructure of polycrystalline materials is a random tessellation. We will focus on the mostly used Laguerre tessellation model based on generators, which form a locally finite point set. Considering the set of generators as a Gibbs point process we obtain the Gibbs-Laguerre tessellation. The choice of the energy function of the underlying Gibbs point process reflects the desired geometrical characteristics of grains. For the statistical analysis of an experimental data we can simulate from a given model using MCMC. The estimation of the parametric model is reasonable only in some range of parameters. We present a method of statistical reconstruction of Gibbs-Laguerre tessellations given real data of a polycrystal.

Xiaoyan Song (Beijing University of Technology)

***3D microstructure and heterogeneous strain response of cemented carbides during deformation***

*Joint with Yanan Li, Xuemei Liu, Jing Fang and Xingwei Liu*

A new method for creating three-dimensional finite element model based on real microstructures of the WC-Co cemented carbides was proposed. A series of simulations were performed to examine the heterogeneous interactions between the pre-existing thermal residual stress and the applied external stress in the cemented carbides. The deformation behavior of the as-sintered cemented carbide was demonstrated in detail for the process of uniaxial compression. The results indicate that among the heterogeneous distributions of the strain and stress in the composite microstructure, the layer-like Co distributing in the transverse cross-section with respect to the direction of compression has the most rapid strain response. The microcracks may preferentially nucleate at these regions due to the fast accumulation of plastic deformation. Assisted by 3D modeling based on both the finite element method and molecular dynamics, new strategies were proposed to achieve ultrahigh fracture strength of the composite material. Further, cemented carbide bulk materials were prepared by sintering the in-situ synthesized WC-Co nanoscale composite powders, which had coherent or semi-coherent interfaces within the cermet particles, and excellent integrated mechanical performance were obtained.

Jon Sporring (University of Copenhagen)

***A generalization of Ripley's  $K$ -function for space curves***

*Joint with Rasmus Waagepetersen and Stefan Sommer*

The first- and second-moment structure of spatial point sets can be characterized by the intensity function and Ripley's  $K$ -function. Given a set of points, the homogeneous  $K$ -function can be estimated from the matrix of all pair-wise distance of the points, also known as the distance matrix. This inspires us to consider the  $K$ -function as a description of distance matrices in general, which implies that for any set of objects and distance functions between them, we can compute the set's distance matrix, and hence we can compute a  $K$ -function. In this work, we consider sets of space curves and some curve-distance and semi-distance functions, we compute  $K$ -functions from their distance matrices, we empirically investigate the resulting  $K$ -functions for their ability to characterize sets of curves that cluster in various ways, and we compare with an existing method from the literature presented in Chiu et al. 2013.

Jakub Staněk (Charles University)

***Similarity of realisations of random sets via their morphological skeletons***

*Joint with Johan Debayle, Vesna Gotovac, Kateřina Helisová and Markéta Zikmundová*

The talk concerns a method of assessing similarity of realisations of random sets based on construction of their morphological skeletons and consequent covering of the realisations by unions of discs with centres on the skeletons. Since the realisations are considered to be binary images, the skeletons together with the corresponding discs can be viewed as marked point processes with specific properties. Different functions for comparing such marked point processes are shown. The described procedure is illustrated on a simulation study with the aim to distinguish between realisations coming from different models.

Mads Stehr (CSGB)

***Asymptotic Variance of Newton-Cotes Quadratures based on Randomized Sampling Points***

*Joint with Markus Kiderlen*

Motivated by the stereological issue of volume estimation from cross-sectional area measurements, we consider the problem of numerical integration when sampling nodes are random, and we suggest to use Newton-Cotes quadrature rules to exploit smoothness properties of the integrand. Compared to the classical Cavalieri estimator based on equidistant sampling, it was shown in previous papers that a Riemann sum approach can cause a severe variance inflation when the sampling

points are not equidistant. However, under some integrability conditions on the typical point-distance, we show that Newton-Cotes quadratures based on a stationary point process in  $\mathbb{R}$  yield unbiased estimators for the integral and that the aforementioned variance inflation can be avoided if a Newton-Cotes quadrature of sufficiently high order is applied. More specifically, we show that the variance of estimators based on  $n$ 'th order Newton-Cotes rules decrease at the same rate as the classical Cavalieri estimator (with decreasing point increment), if the integrand is a so-called  $(n, 1)$ -piecewise smooth function.

By simulations we illustrate the variance improvement of the trapezoidal rule and Simpson's rule for functions with varying smoothness properties.

Torben Steiniche (Aarhus University Hospital)

*Digital pathology – what to come in the future*

There are 3 overall trends in pathology, that will have major influence on the specialty in the near future:

1. From Microscope to monitor (digital pathology)
2. From Morphology to molecule (next generation frequency, NGS)
3. From Manual to Machine (automatization of the laboratories)

This future will not only be a digitalization of our slides but the combination of digitalization with image analysis and artificial intelligence enabling us to:

1. Automated and objective quantification of immunohistochemical stainings.
2. Guided microscopy and even automated diagnosis on routinely stain slides (H&E slides).

The presentation will give some examples of these major trends in pathology and how these trends will be combined in a whole new future for pathology.

Robert A. Sweet (University of Pittsburgh)

*Hard of Listening: Auditory Cortex Pathology in Schizophrenia  
(Stereologically (Un?) Informed Studies of Auditory Cortex in Schizophrenia)*

It has long been known that impaired auditory sensory processing and impaired auditory physiology are present in subjects with schizophrenia. An ongoing debate regarding these *in vivo* sensory impairments found within individuals with schizophrenia was whether they might arise solely from impairments in "higher order" brain regions that lead to failed sensory processing (top down impairments), or whether primary deficits in sensory processing may make independent contributions to deficits (bottom up impairments). To resolve this issue, my lab

undertook a series of studies to directly examine structural and molecular pathology in this brain region in individuals with schizophrenia. In a series of studies conducted using both biased designs and design-based stereology, we have identified reductions in density and number of dendritic spines in primary auditory cortex in several independent cohorts and have confirmed that this is due to reduction in only the smallest spines. Importantly, these impairments did not result from neuron loss in primary auditory cortex, nor were they recapitulated by long-term antipsychotic exposure in an animal model. These studies have further identified alterations in MAP2 protein that may serve as a common downstream hub for auditory cortex impairments of dendritic morphology. These findings have strongly impacted the field of schizophrenia neuroscience. Our demonstration of cellular and molecular pathology within primary sensory cortex firmly excluded a monolithic “top down” viewpoint. It is no longer tenable to argue that sensory impairments in this illness arise in the absence of sensory system pathology.

Yong Tang (Chongqing Medical University)

*Effects of fluoxetine on the cognitive function, neurons and synapses in the hippocampus of APP/PS1 transgenic mouse model of Alzheimer's disease*

*Joint with Chun-ni Zhou, Yi Zhang, Lin Jiang, Feng-lei Chao, Lei Zhang and Jing Ma*

**Introduction:** It has been reported that fluoxetine (FLX) shows positive effects on the AD patients who have depression and anxiety. It is unclear, however, whether FLX can affect the pathogenesis of early AD. To address this issue, we designed the present study. The present study is the first study to investigate the effects of FLX on the neurons and synapses in the hippocampus of early APP/PS1 transgenic AD mice using the unbiased stereological techniques and other techniques.

**Methods:** 8-month-old male APP/PS1 mice were randomly divided into an APP/PS1 + NS group and an APP/PS1 + FLX group. 8-month-old male wild-type (WT) littermates were randomly divided into a WT + NS group and a WT + FLX group. The mice in the WT + FLX group and APP/PS1 + FLX group were intraperitoneally injected daily with FLX (10 mg kg<sup>-1</sup> i.p. dissolved in 0.9% NS) regime for 10 weeks. The mice in the WT+NS group and APP/PS1+NS group were intraperitoneally injected daily with NS (equivalent 0.9% NS i.p.) for 10 weeks. At last two weeks injection, the spatial learning and memory ability of the mice was detected with Morris water maze. After 10 weeks, 6 mice were randomly selected from each group. The total numbers of the neurons, immature neurons and synapses were estimated with the unbiased stereological methods. The newborn neurons and 5HT4R<sup>+</sup>/NeuN<sup>+</sup> cells in the hippocampal subregions were counted with immunofluorescence technique. Immunofluorescence was used to detect the changes of amyloid plaques, 5HT1A receptor and the density of PSD95 in the hippocampus of each group mice. The changes of phosphorylated Tau protein, the levels of GSK3 $\beta$  and p-ser9-GSK3 $\beta$  and the levels of SYP and BDNF in the hippocampus of each group mice were detected with ELISA technique.

**Results:** 10 week FLX treatment could delay the decline progress in the learning and memory ability of early AD mice. FLX treatment could not only significantly decrease the amyloid plaques and  $A\beta_{40}$  and  $A\beta_{42}$  in the hippocampus of early AD, but also reduce the expression levels of GSK3 $\beta$  and phosphorylated Tau protein and inhibit the activity of GSK3 $\beta$ . At the same time, FLX treatment could also increase the expression of 5HT1A receptors in the neurons of hippocampus. FLX might increase the expression of 5HT1A receptors in the neurons of hippocampus or activate the 5HT1A receptors, decrease the expression level of GSK3 $\beta$  and inhibit the activity of GSK3 $\beta$ , thereby reducing the production of  $A\beta_{40}$ ,  $A\beta_{42}$  and phosphorylate Tau protein in the hippocampus of early AD. 10 week FLX treatment could delay the volume shrinkage of DG and CA1/2 of hippocampus in early AD mice. FLX treatment could delay the loss of neurons in DG and CA1/2 regions of hippocampus in early AD mice, and FLX treatment could significantly increase the number of newborn neurons in DG, CA1/2 and CA3 regions of hippocampus in early AD mice. FLX treatment could significantly increase the number of immature neurons in DG region of hippocampus in early AD mice. FLX treatment could significantly increase the number of 5HT4<sup>+</sup>/NeuN<sup>+</sup> cells in DG, CA1/2 and CA3 regions of hippocampus in the early AD. FLX might promote the neurogenesis through increasing the 5HT4 receptor expression or activating the 5HT4 receptors in the neurons of the hippocampus in early AD. There was a large number of dendritic spine loss in the DG, CA1/2 and CA3 regions in the hippocampus at 10 months APP/PS1 mice, suggesting that the dendritic spines change in the hippocampus may be related to cognitive function decline of early AD. 10-week FLX treatment could delay the loss of dendritic spines in the DG, CA1/2 and CA3 regions of the hippocampus in early AD and increase the density of PSD95 in the DG, CA1/2 and CA3 regions of the hippocampus. 10-week FLX treatment could delay the expression level decline of SYP in the hippocampus of early AD. 10-week FLX treatment could delay the expression level decline of BDNF in the hippocampus of early AD. FLX could delay the synapse change possibly through BDNF and 5HT4 receptors, which might strongly provide a scientific foundation for the further studies on the mechanism for the effect of FLX on early AD.

**Conclusions:** The present results indicated that FLX treatment could protect the neurons and synapses in the hippocampus of early AD through 5-HT system, which might be the important structural bases for the FLX-induced improvement of the spatial learning and memory ability of early AD. Moreover, our results suggested that the FLX may be a safe and effective drug for delaying the progress of AD, which might provide a starting point for further research into the new preventative measures and treatments of AD.

Santiago Velasco-Forero (MINES ParisTech)

***On approximating mathematical morphology operators via deep learning techniques***

*Joint with B. Ponchon, S. Blusseau, J. Angulo and I. Bloch*

Mathematical Morphology (MM) is a well-established discipline whose aim is mainly to provide tools to characterise complex object via their shape/size features. This study addresses the problem of robust approximation of mathematical morphology (MM) operators by deep learning methods. We present two cases, (a) Asymmetric autoencoders for part-based approximations of classical MM in the sense of [1] and, (b) image-to-image translation networks [2] to produce robust MM operators in presence of noise.

*References*

- [1] Ponchon B., Velasco-Forero S., Blusseau S., Angulo J. and, Bloch I., Partbased approximations for morphological operators using asymmetric autoencoders, *ISMM'19*, 2019
- [2] Isola P., Zhu J-Y, Zhou T. and, Efros A., Image-to-Image Translation with Conditional Adversarial Networks, *CVPR'17*, 2017.

András E. Vladár (NIST)

***Atomically Accurate 3D Measurements on Nanometer-size Structures by HR-SEM and Modeling***

The best high-resolution scanning electron microscopes (HR-SEMs) today can focus the electron beam into a sub-0.5 nm spot that – in principle - allows for measurements with atomic resolution. Special stages permit taking images from as many angles as needed for the reconstruction of the three-dimensional (3D) shape of the sample. Nevertheless, the accurate determination of the 3D shape at the nm-scale is not trivial: the signals of the SEM are the results of complex interactions and the luminance values of its images do not represent sample dimensions directly. A 1 nm diameter Si sphere has only 26 atoms in a volume of about  $0.4 \text{ nm}^3$ . Because the smallest nanometer-scale features consist of a small number of atoms, which can generate only weak signals, atomic level SEM measurements must be fully optimized for the measurand, i.e., the information sought.

Recently, cryogenic transmission electron microscopy (TEM) has achieved unprecedented, atomic resolution in 3D measurements of protein molecules and other biological structures [1]. Other TEM measurement techniques are also available for nanoparticle 3D reconstruction [2]. Due to the nature of the transmitted electron signal, TEM images show inner structures of the sample chiefly, while the SEM shows mainly the surface, therefore the various SW methods for 3D TEM measurements are not directly applicable to SEM imagery.

The SEM secondary electron signal contains 3D information that – with suitable software – can be used for shape reconstruction. Even a single top-down image can be sufficient for simple structures. Some of the best, model-based size and shape SEM measurements of 10 nm size objects have achieved measurement uncertainty of 0.1 nm, i.e., only a few atoms [3]. These SEM measurement results match that of TEM and x-ray scatterometry. For complex samples, images taken from more than one vantage point are necessary.

As the signal generation in the SEM is fairly complex, accurate, physics-based simulation methods, like NIST JMONSEL are necessary to deduce the 3D shape of the sample. A great deal of improvement is possible both in the determination of the best measurement conditions (see Figure 1 as illustration) and in the analysis and interpretation of the measured raw data. For very accurate atomic scale measurements, high-throughput, high-resolution laser interferometry is indispensable to compensate for the nm-scale unwanted motions of the sample.

This contribution will present our progress in nm-scale 3D SEM measurements and identify the needs and possibilities for an international cooperation to usher in the widespread use of computational scanning electron microscopy along with fully optimized, significantly improved, atomic-resolution 3D measurements and new, higher performance SEMs.

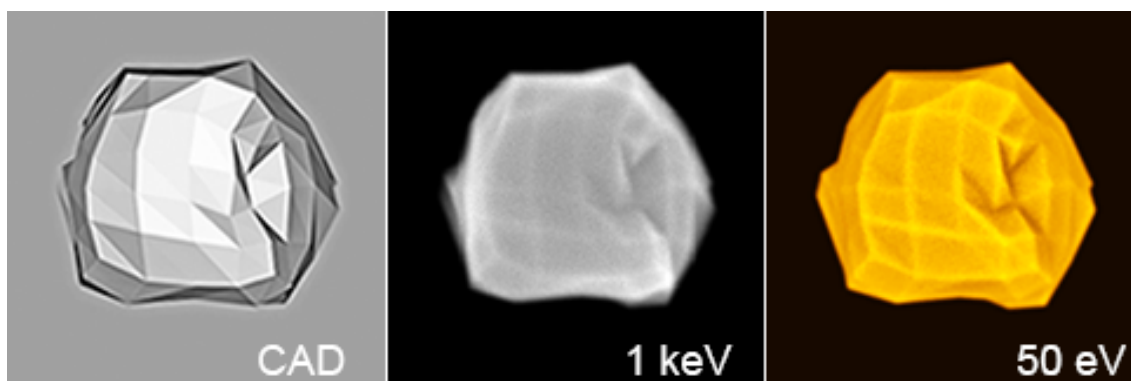


**Figure 1:** Monte-Carlo-simulated 3D secondary electron images of a 60-nm size Au nanoparticle: computer-assisted design (CAD) model, and 1 keV and 50 eV landing energy images. The lower landing energy electron beam generates images that are more suitable for atomic-resolution 3D reconstruction.

Contributions of the National Institute of Standards and Technology are not subject to copyright. Mention of commercial products or services here does not imply approval or endorsement by NIST, nor does it imply that such products or services are necessarily the best available for the purpose.

### References

- [1] <https://doi.org/10.1038/nature.2017.22738>
- [2] <https://doi.org/10.1016/j.micron.2016.09.010>
- [3] <https://doi.org/10.1117/12.2045977>

Matthias Weber (Ulm University)

***Automatic detection of amyloid fibril crossovers in cryo-EM image data, using a combination of conventional image processing and machine learning***

*Joint work with A. Bäuerle, M. Schmidt, M. Neumann, M. Fändrich, T. Ropinski and V. Schmidt*

Soluble proteins can form insoluble fibers which assemble into so-called amyloid fibrils. Amyloid fibrils are periodically shaped helical structures which cause a group of diseases called amyloidosis when accumulating in organs. Depending on the affected organ, various diseases and symptoms can arise, e.g., heart arrhythmia, kidney disease or Alzheimer's.

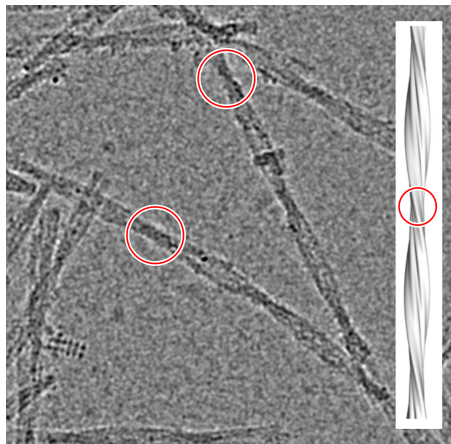


**Figure 1:** Sample image data of amyloid fibrils obtained by cryo-EM. Segments where the fibril is oriented orthogonal to the image plane, so-called crossovers, are highlighted. Additionally, we show the 3D helical structure of fibrils, leading to the observation of a periodically varying width in 2D.

When observing fibrils using microscopy techniques like cryogenic electron microscopy (cryo-EM), the helical structure results in a seemingly irregular fiber with a periodically varying width. Detecting sections of minimal width (crossovers, see Figure 1) enables us to obtain the pitch of the helix, i.e., the length of a complete turn, by computing the distance between two consecutive crossovers. This is an important characteristic for the analysis of amyloid fibrils.

However, the labeling of crossovers by hand is a time-consuming and error-prone task. We present a method for the automatic extraction of crossovers from 2D image data obtained by cryo-EM. Direct application of convolutional neural networks (CNNs) similar to the U-Net leads to good results when sufficiently good training data is available. In our case, however, many labels are missing in the training data. This leads to various problems which make a direct training and application of a CNN infeasible.

Classical tools of image analysis and pattern recognition like Hough transform and clustering algorithms based on geometric graphs help to mitigate these problems. Thus, we combine classical tools of image analysis and pattern recognition for pre- and postprocessing with machine learning techniques to achieve good results.

Daniel Westhoff (Ulm University)

***Reconstruction and stochastic 3D modeling of grain boundaries in polycrystalline materials from incomplete data, using tessellations with flat and curved facets***

*Joint with Lukas Petrich, Jakub Staněk, Mingyan Wang, Carl E. Krill III and Volker Schmidt*

Polycrystalline materials are composed of a space-filling system of so-called grains. The microstructure of polycrystalline materials, i.e., morphological properties of the grains, plays a key role for physical phenomena such as grain growth. Full information about the shape of the grains can be acquired, e.g., by three-dimensional electron backscatter diffraction (3D-EBSD), whereas by far-field three-dimensional X-ray diffraction (3D-XRD) microscopy the only geometrical information that can be obtained are the centers of mass and volumes of each grain. The advantage of the latter measurement technique is that it allows to quickly investigate large numbers of grains without destroying the specimen in the process, rendering it a good solution for in situ experiments.

In this talk, a method to predict the full 3D information of the grain system, based on a 3D-XRD measurement is presented. We assume that the system of grains can be represented as a *Laguerre tessellation*, which is a space-filling system of convex polytopes. Laguerre tessellations can be generated by points with real-valued marks. From the information about centers of mass and volumes of grains, we construct such a system of marked points, which acts as a generator for a Laguerre tessellation. The system of marked points is iteratively refined such that the centers of mass and volumes of the polytopes in the Laguerre tessellation approximately correspond to the values obtained from the 3D-XRD measurement.

So far, we have assumed that the grain boundaries are flat, such that we can model the grains as convex polytopes. However, for some materials, the boundaries may be curved. In this case, the concept of a Laguerre tessellation can be adapted to generate a space-filling system of non-convex grains. This can, e.g., be done using the *spherical growth tessellation*, which can also be generated from a system of marked points. We present a stochastic 3D model for polycrystalline AlCu samples based on a spherical growth tessellation. By the aid of this model, virtual polycrystalline microstructures can be generated, the statistical properties of which approximately match the ones extracted from 3D image data of real microstructures. In addition, by a systematic variation of model parameters, virtual polycrystalline materials with different morphological properties can be generated. These structures can, e.g., be used as input for simulations of grain growth in polycrystalline materials.

Dvoralai Wulfsohn (Geco Enterprises Centro de I+D; Dayenu Ltda)

***Pronofrut: IT-assisted Stereology for Monitoring Orchards for Precision Horticulture***

*Joint with Jonathan E. Gardi, Oded Cohen, Marta Garcia-Fiñana and Ines Zamora*

Pronofrut™ is a crop monitoring service developed for the fruit, winery and horticultural industries which incorporates a stereological sampling methodology supported by Information technologies to optimise sampling, data collection and processing. Originally developed with yield estimation as the primary objective, it has evolved to provide tools and techniques for providing key information required to implementing precision management of orchard and horticultural crops. Such information includes georeferenced maps of plant characteristics and fruit loading, early detection of infection by botrytis and other molds, evaluation of labour quality, evaluation of the distribution of fruit quality and maturity, and yield estimation.

Although commercial fruit trees are genetically uniform, because both the root stock and the scion/cultivar are of clonal origin, due to variations in many orchard conditions there may be large variations in tree yield, providing a challenge for accurate estimation. Early forecasting of crop yield is important for market planning and for growers and exporters to plan labor, bins, storage and purchase of packing materials. Modern orchard management for high value production, such as fruit for export and quality wines, involves the manipulation of individual tree canopies and even individual fruit. Thus, the ability to conduct rapid, timely evaluations of the quality of tasks such as pruning and thinning of trees and fruit is also fundamental for delivering quality and costs and correcting errors early on.

The general procedure is:

1. A high resolution, georeferenced image of the orchard is derived from images obtained using an unmanned aerial vehicle (UAV) equipped with specialized cameras. Alternatively, maps may be obtained using optical sensing from ground-based vehicles.
2. OrchardMapper software uses image analysis of the orchard images to detect individual plants and their characteristics, and quantify the spatial variability of the plantation as derived from visible features in images. This information is input to an algorithm that selects the sample trees, with selection designs depending on the objective of the sampling, and also provides a prediction of the contribution to estimation error from the tree sample.
3. Manual fruit counts and size (diameter, volume or mass) measurements are made on small samples of fruit selected systematically uniformly at random (a fractionator design) across the plantation. Low counts are important to reduce human errors in counting. The selection of samples are made following unbiased sampling and counting rules. A smartphone app (Pronofrut

Sampler) is used to guide sampling indicating to the user the exact position of the sample, and also to input data and, at the end of a survey, upload the data to a server for processing. The application saves a position and timestamp for each sample, permitting the creation of maps of the orchard.

4. The sample counts and measurements are used to estimate yield and distributions of quality parameters and a semi-empirical variance model is used to predict the error of the yield estimate.
5. If the variance model predicts an error that exceeds the target precision (typically less than 10% at field scale), a supplemental sample may be taken as guided by the app.

Steps 1–2 are optional, but provide a way to optimize tree sample selection and reduce the cost of the survey.

We present Pronofrut with a special emphasis on the IT assisted aspects, namely the OrchardMapper software for individual plant detection from images, the selection of tree samples and variance prediction, and the Sampler application for in-field manual counting and sampling.

We will also present results of yield forecasts carried out at the commercial scale for several species, including comparisons of the true error with the model-predicted error, where the ‘true error’ is derived as the difference between the estimated yield and the yield reported by the packing house.

# **Part III**

## **Posters**

Abdel-Rahman Al-Absi (Aarhus University; CSGB)

***GABA(A) receptor  $\alpha 3$  subunit deficit in the prefrontal cortex of Df(h22q11)/+ genetic mouse model of schizophrenia***

*Joint with Per Qvist, Simon Glerup, Connie Sanchez and Jens R Nyengaard*

**Background:** Schizophrenia is a highly heritable neuropsychiatric disorder that disturbs patient's thoughts, feelings and behavior, resulting in a 2–3 fold increase in their mortality rate. Although the etiology is poorly understood, emerging candidate risk genes for schizophrenia, along with clinical findings, implicate various aspects of GABAergic neurotransmission with the cognitive symptoms of schizophrenia.

**Methods:** Through behavioral, molecular, biochemical, and brain morphometric characterization of a new genetic mouse model of schizophrenia Df(h22q11)/+ which mimics the 22q11.2 human microdeletion syndrome, we investigate dysfunctions in the cortical GABAergic system with potential translational relevance to schizophrenia.

**Results:** Df(h22q11)/+ shows a decrease at both mRNA and protein levels of GABA(A)  $\alpha 3$  receptor subunit in the prefrontal cortex (PFC). This decrease is accompanied with deficits in both sensory motor gating and visuospatial memory.

**Conclusion:** Further investigations are necessary to explore the impact of the GABA(A)  $\alpha 3$  on both the inhibitory and the excitatory circuits in PFC of Df(h22q11)/+ mice.

Stine Andersen (Aarhus University Hospital)

***Effects of combined angiotensin II receptor antagonism and neprilysin inhibition in experimental pulmonary hypertension and right ventricular failure***

*Joint with Julie Birkmose Axelsen, Steffen Ringgaard, Jens Randel Nyengaard, Janus Adler Hyldebrandt, Harm Jan Bogaard, Frances S. de Man  
Jens Erik Nielsen-Kudsk and Asger Andersen*

**Background:** Combined angiotensin II receptor antagonism and neprilysin inhibition by LCZ696 reduces morbidity and mortality in heart failure patients and works by reducing RAAS activity and increasing cGMP levels. This study aims to evaluate the effects of LCZ696 in rats with pulmonary hypertension and right ventricular (RV) failure.

**Methods and results:** Pulmonary hypertension was induced in rats ( $n = 34$ ) by combined exposure to the vascular endothelial growth factor-receptor antagonist SU5416 and hypoxia (SuHx). To distinguish pulmonary vascular from cardiac effects, isolated RV failure was induced by pulmonary trunk banding (PTB) in another group of rats ( $n = 40$ ). In both models, the development of RV dysfunction

was verified before randomization to treatment with LCZ696 (60 mg/kg/day) or vehicle for five weeks. Hemodynamic effects were evaluated by echocardiography, MRI scans, and invasive pressure-volume measurements, while pulmonary vascular and RV remodeling was evaluated by stereology.

In the SuHx rats, LCZ696 treatment reduced the increase in RV pressure and the development of RV hypertrophy and RV dilatation compared with vehicle treatment. LCZ696 also reduced remodeling of the smaller pulmonary arteries. In the PTB rats, LCZ696 treatment did not have any effects on RV hypertrophy or function.

**Conclusions:** Combined angiotensin II receptor antagonism and neprilysin inhibition reduced RV systolic pressure, hypertrophy and dilatation in rats with pulmonary hypertension. These effects seem secondary to pulmonary vascular changes, including reduced pulmonary vascular remodeling, as similar effects were not seen in rats with isolated RV failure.

John M. Basgen (Charles R. Drew University of Medicine and Science)

*Determination of Sample Size for Counting Podocytes using the Fractionator/Disector*

*Joint with Felipe Garzon, Khadija Banu and Madhav C. Menon*

**Introduction**

Kidney diseases affect near half a billion people with few therapeutic options other than kidney transplantation or dialysis. The functional unit of the kidney is the nephron composed of a glomerulus and its tubule (Figure 1). The human kidney has approximately one million glomeruli. The glomerulus is a network of capillaries where impurities in the blood as well as a large amount of water and useful metabolites are filtered across the capillary walls. The filtrate exits the glomerulus and travels through an extensive tubular system (Figure 1) where much of the filtered water and useful metabolites are absorbed resulting in urine.

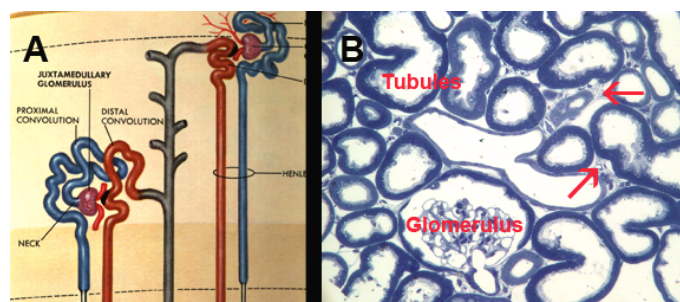


**Figure 1:** A. 3-D drawing of the outer portion of a kidney showing two spherical glomeruli (in purple) and their associated tubules (in blue and brown). B. 2-D microscopic image of a 1- $\mu$  thick section of kidney showing a glomerulus, numerous surrounding tubules and the interstitial space (red arrows) between the tubules.

The glomerulus contains three types of cells. The endothelial cells line the inside of the capillary walls and sit on the glomerular basement membrane. The epithelial cells, known as podocytes, are attached to the glomerular basement membrane on the outside of the capillary walls. The mesangial cells occupy the space between the glomerular capillaries (Figure 2). The podocyte has been shown to be the primary target of many kidney diseases and the focus of much research during the past decade.

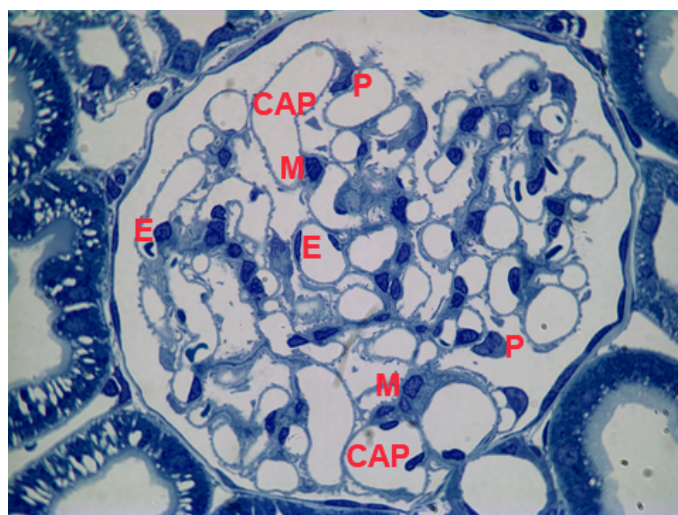


**Figure 2:** A glomerulus showing capillary lumens (Cap), podocytes (P), endothelial cells (E) and mesangial cells (M).

An early marker of kidney disease is protein in the urine that may indicate the need for a kidney biopsy. A biopsy can confirm disease by showing pathological changes to glomeruli and/or tubules and interstitium. The loss of more than 20% of podocytes may indicate chronic kidney disease leading to complete loss of kidney function [1]. Glomerular sclerosis, tubular atrophy and interstitial fibrosis (scarring) are common endpoints in progressive renal diseases from diverse etiologies. Shroom3 is a protein needed for normal development of several organs including the kidney. Recently it has been shown that a mutation in the Shroom3 gene leads to an overproduction of the collagen protein in the tubule and is associated with loss of kidney function. Surprisingly, patients with the same Shroom3 mutation may be protected from proteinuria suggesting a protective role in the glomerular compartment [2].

To try to understand this dichotomy associated with the Shroom3 mutation, the negative effect on tubule function and a positive effect on glomerular function, mouse experiments were designed to study these effects on glomeruli and tubules. Besides studying the metabolic pathways related to the Shroom3 mutation, structural parameters such as glomerular volume and podocyte number will be studied.

Glomeruli, the cells and the nuclei within the cells are 3-dimensional (3-D) particles but we use 2-dimensional images of these particles to measure structure

necessitating the use of stereological tools to carry out the relevant measurements. We will use the Fractionator/Disector [3] tool to count the number of podocytes per glomerulus. Two key questions to be answered before the start of a morphometric study in the kidney are: (1) How many animals are needed per experimental group; and (2) How many glomeruli per animal need to be measured. To answer the first question a power analysis is required, which will not be discussed here. In this report we will demonstrate how we answered the second question for our future study. Measuring too few glomeruli would result in too imprecise an estimate and measuring too many glomeruli would result in a waste of time and money. In a previous study we used the Fractionator/Disector tool to count podocytes and the data from that study was available for analysis to help determine the optimal number of glomeruli to study per kidney.

## Methods

**The Fractionator:** BALB/c mice age two months were sacrifice and a portion of kidney was fixed in glutaraldehyde and embedded in plastic. An ultramicrotome was used to cut 200 sequential 1- $\mu\text{m}$  thick sections from a tissue block with every 10th section saved to a slide. Thus 1/10 was the fraction of sections from a glomerulus that were saved for analysis. Only glomeruli beginning after the first section of the 200 sequential sections and ending before the 200th section were analyzed. This is the Fractionator principle.

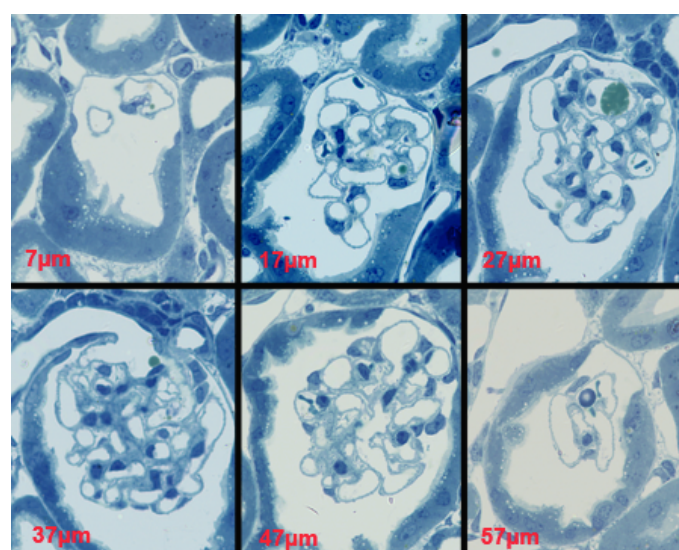


**Figure 3:** The Fractionator. Six sections through one glomerulus evenly spaced 10  $\mu\text{m}$  apart. The first section is random within the first 10 micrometers of the beginning of the glomerulus. In this example the 7th section was the first saved section. Every subsequent 10th section was saved to a slide resulting in an unbiased systematic sample of the glomerulus.

**The Disector:** The boundary of podocytes is not resolvable when using the light microscope. Therefore we used the number of podocyte nuclei as a surrogate for

the number of podocytes assuming there is one and only nucleus per podocyte. Glomeruli as well as podocyte nuclei are 3-D particles, but in 2-D images we do not see 3-D glomeruli or nuclei, we see 2-D profiles from the glomeruli and nuclei. The number of profiles seen in a 2-D image is not directly related to the number of particles present in 3-D space. This is known as the Wicksell Problem [4]. The Wicksell Problem was solved with the introduction of the Disector probe by D. C. Stereo [5].

The Disector states that the numerical density of particles in 3-D space can be estimated without bias using a pair of sections, a known distance apart, and counting the number of profiles from particles present in the Reference section but not present in the Look-up section. The numerical density is estimated by the equation:

$$\text{Numerical density} = 1/(d \times \text{Area}) \times \sum Q^-$$

where  $d$  is the distance between the two sections, Area is the area of the Reference section, and  $\sum Q^-$  is the sum of profiles counted from nuclei present in the Reference section but not present in the Look-up section.

**The Fractionator/Disector:** We combined the Disector probe with the Fractionator (Fractionator/Disector) to count podocyte nucleus profiles. When using the Fractionator/Disector one does not need to know the distance between the sections and the number of particles are counted directly not the numerical density as when only using the Disector. To use the Disector two sections were needed. Thus every 10th section was collected (the Reference Section) for the Fractionator and the preceding adjacent section was collected and saved (the Look-up Section). Then profiles from podocyte nuclei seen in the Reference Section but not in the Look-up section were counted (Figure 4).

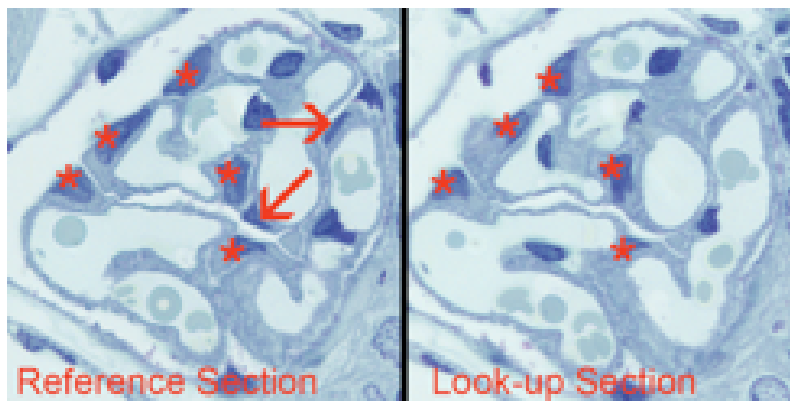


**Figure 4:** Disector. Profiles of podocyte nuclei present in both sections are marked with a red asterisk and not counted. Two profiles from nuclei in the Reference Section but not present in the Look-up section are counted and labeled 1 and 2.

The estimate of number of podocytes per glomerulus is calculated with the equation:

$$\text{Podocyte number} = 10 \times \sum Q^-$$

where 10 is the reciprocal of the fraction of the glomerulus sampled and  $\sum Q^-$  is the sum of profiles counted from nuclei present in the Reference Section but not present in the Look-up Section.

## Results

The number of podocytes counted in each of 7 glomeruli from five animals was available for analysis (Table 1).

After measuring a structural parameter such as podocyte number for several animals in an experimental group, a mean and standard deviation (SD) for the group can be calculated. Dividing the SD by the mean is the coefficient of variation for the group. Within each animal of the group measurements are made in multiple glomeruli and a mean and SD of the parameter for each individual animal can also be calculated. Dividing this within animal SD by the square root of the number of glomeruli measured for the animal is the standard error (SE) for the animal. A coefficient of error (CE) is obtained by dividing the SE by the mean for the animal. This can be repeated for each of the animals in the group (Table 1).

The calculated coefficient of variation for the group is referred to as the observed coefficient of variation (OCV). The OCV can be divided into two components the biological variation (CV) among the animals in the group and the variation among the glomeruli within each animal. If the OCV is perceived to be too large it may be decreased by doing more work (measuring more glomeruli per animal). Before measuring more glomeruli, an expensive task, one can determine if measuring more glomeruli per animal is useful. If most of the variation of the OCV is the biological variation among the animals, measuring more glomeruli per animal will not reduce the OCV very much. However if much of the variation of the OCV is among the glomeruli within each animal, then measuring more glomeruli will reduce the CE and the OCV. The relationship among OCV, CV, and CE is given by:

$$OCV^2 = CV^2 + CE^2$$

We can use the average  $CE^2$  for the animals in the group in the equation. Insert the values for  $OCV^2$  and the average  $CE^2$  into the equation and solve for  $CV^2$ . Solve for  $CV^2$ . If  $CV^2$  is larger than  $CE^2$ , measuring additional glomeruli will not decrease the OCV much, but if  $CE^2$  is much larger than  $CV^2$  then adding glomeruli will decrease  $CE^2$ .

For our data the average  $CE^2$  for the five animals was 0.0167, and the  $CV^2$  was 0.0011 (Table 1).  $CE^2$  is much larger than  $CV^2$  meaning the variation among glomeruli within an animal is much greater than the biological variation among the animals. To decrease the  $CE^2$  and move it to more closely match the  $CV^2$ , the number of glomeruli per animal should be increased. We double the number of glomeruli per animal, and then repeated the analysis (Table 2). The new average  $CE^2$  was 0.0077 and the  $CV^2$  0.0162. Now the  $CE^2$  is slightly less than the  $CV^2$ . And measuring more glomeruli per animal would not be cost effective.

## Abstracts for posters

**Table 1**

	Number of Animal Podocyte	Glom 1	Glom 2	Glom 3	Glom 4	Glom 5	Glom 6	Glom 7	Glom 8	Glom 9	Glom 10	Glom 11	Glom 12	Glom 13	Glom 14	Animal Mean	Animal SD	Animal SE	Animal CE	Animal CE <sup>2</sup>
1	95	90	140	140	60	60	115	60								95	37	14	0.1466	0.0215
2	99	70	75	115	130	105	90	110								99	22	8	0.0833	0.0069
3	90	88	125	50	155	60	60	90								90	38	15	0.1618	0.0262
4	71	55	115	85	60	100	53	30								71	30	11	0.1587	0.0252
5	79	95	75	70	90	58	78	90								79	13	5	0.0625	0.0039
Group Mean	86.6								OCV <sup>2</sup> =	CV <sup>2</sup> +	CE <sup>2</sup>								Average CE <sup>2</sup>	0.0167
Group SD	11.6								0.0178 =	CV <sup>2</sup> +	0.0167									
OCV	0.13								0.0178 =	0.0011 +	0.0167									
OCV <sup>2</sup>	0.0178																			

**Table 2**

	Number of Animal Podocyte	Glom 1	Glom 2	Glom 3	Glom 4	Glom 5	Glom 6	Glom 7	Glom 8	Glom 9	Glom 10	Glom 11	Glom 12	Glom 13	Glom 14	Animal Mean	Animal SD	Animal SE	Animal CE	Animal CE <sup>2</sup>
1	100	90	140	140	60	60	115	60	100	150	150	70	70	125	70	100	36	10	0.0956	0.0091
2	104	70	75	115	130	105	90	110	80	85	125	140	115	100	120	104	22	6	0.0555	0.0031
3	85	88	125	50	155	60	60	90	78	115	40	145	50	50	80	85	37	10	0.1176	0.0138
4	74	55	115	85	60	100	53	35	60	120	90	65	105	58	35	74	28	8	0.1021	0.0104
5	77	95	75	70	90	58	78	90	90	70	65	85	53	73	85	77	13	3	0.0448	0.0020
Group Mean	88.0								OCV <sup>2</sup> =	CV <sup>2</sup> +	CE <sup>2</sup>								Average CE <sup>2</sup>	0.0077
Group SD	13.6								0.0239 =	CV <sup>2</sup> +	0.0077									
OCV	0.15								0.0239 =	0.0162 +	0.0077									
OCV <sup>2</sup>	0.0239																			

## Conclusion

For our future studies of podocyte number and podometrics using BALB/c mice to study the effects of the Shroom3 mutation and SHROOM3 protein we will use the Fractionator/Disector method and 14 glomeruli per animal.

*This report is dedicated to D. C. Sterio on the 35th anniversary of the introduction of the Disector.*

## References

- [1] Wharram BL, Goyal M, Wiggins JE, et al, (2005) Podocyte depletion causes glomerulosclerosis: diphtheria toxin-induced podocyte depletion in rats expressing human diphtheria toxin receptor transgene. *J Am Soc Nephrol* 16: 2941–2952.
- [2] Wei Chengguo, Banu K, Garzon F, et al, (2018) SHROOM3-FYN interaction regulates nephron phosphorylation and affects albuminuria in allografts. *J Am Soc Nephrol* 29: 2641–2657.
- [3] Gundersen HJG, (1986) Stereology of arbitrary particles. A review of unbiased number and size estimators and the presentation of some new ones, in the memory of William R. Thompson, *J Microsc* 143:3–45.

- [4] Wicksell SD, The corpuscle problem. A mathematical study of a biometric problem. *Biometrika* 17: 84–99.
- [5] Sterio DC, (1984) The unbiased estimation of number and sizes of arbitrary particles using the disector. *J Microsc* 134:127–136.
- [6] Howard CV, Reed MG, (1998) *Unbiased Stereology Three-dimensional Measurement in Microscopy*, BIOS Scientific Publishers Limited, 158–165.

Fenghua Chen (Aarhus University)

***Hippocampal volume and cell number in depression, schizophrenia, and suicide subjects***

*Joint with Aksel B. Bertelsen, Jens R. Nyengaard, Raben Rosenberg and Karl-Anton Dorph-Petersen*

Substantial evidence suggests that structural plasticity in the hippocampus may play an important role in the pathophysiology of psychiatric disorders, especially major depressive disorder (MDD) and schizophrenia. Also, *in vivo* imaging studies indicate that the volume of hippocampus may be reduced in both disorders. The aim of the present study is to investigate if depression, schizophrenia or suicide is associated with reduced volume of the hippocampal formation and/or changes in the numbers of neurons and/or glial cells in the different subregions of the hippocampus.

The study is based upon postmortem brain samples from 10 subjects with schizophrenia, 8 subjects with major depression, 11 suicide subjects with a history of depressive disorder, and 10 control subjects with no history of psychiatric or neurological diseases. The microscopic analysis is based on state of the art design-unbiased stereological techniques: the Cavalieri estimator is used to estimate the volume of hippocampus and its subregions, and the optical fractionator method is used to estimate the total number of neurons and glial cells in the individual cell layers in four main regions of hippocampus: the granular cell layer, hilus, CA2/3, and CA1.

We found the volume and the number of neurons and glial cells were similarly reduced by approximately 20% to 35% in depressed and schizophrenia subjects relative to control subjects across all hippocampal regions. In suicide subjects, we only found increased neuron number in CA2/3 subregion.

The volume and number of cells are reduced in depressed and schizophrenia subjects relative to control subjects across all hippocampal regions. Our findings imply that the hippocampus may be a common site of pathophysiology in depression and schizophrenia. Suicide subjects may have a different neurobiology in hippocampus compared to subjects dying with MDD without suicide.

Aneta Gądek-Moszczak (Cracow University of Technology)

***Measuring an angle of the curvature of the spine with scoliosis on X-rays images***

*Joint with Paulina Galkowska and Barbara Jasiewicz*

The work aims to propose a semi-automatic algorithm for calculation the Cobb's angle of the spines with scoliosis. The Cobb angle is used to assess the stage of the spine's deformation and is indicated on the X-ray images manually.

A proposed semi-automatic method for calculation the Cobb's angle was tested on the X-ray images presented children's spine with a different stage of scoliosis. Images were acquired as an element of routine treatment control, allowing to assess the results of treatment. Test images were acquired in the University Orthopedics and Rehabilitation Hospital in Zakopane. Radiograms show the spines of children with different types of scoliosis (scoliosis, kyphosis). Analysed radiographs had a relatively low quality due to high noise, and visible other anatomical parts aside from spine, such as ribs, what complicated the detection of the vertebral column. Radiographs of the spine were used in the posterior-front position. X-ray images have been appropriately processed using basic image transformation operations to remove noise, interference and unnecessary information.

The applied transformations are a median filter, histogram alignment, binarization, morphological gradient. The spine was described with the polynomial of the 5th degree (fig. 1, 2). Centroids were calculated using the  $k$ -means method. Based on this polynomial, the Cobb angle calculation was made using the straight-line equation passing through two points. The input data to the algorithm are the starting points in the places of the most significant span deflections from the  $y$ -axis. A function was created to generate these points according to the normal distribution, assuming as the peak the points giving the results closest to the measured manually. This affects the measurement error and spread of the Cobb angle values between the starting points in the closest neighbourhood. The occurrence and error value is reproducible for different pictures. The algorithm developed to calculate the Cobb angle can be used in diagnosing the progress of treatment. The calculated Cobb angle must, however, be treated as an angle with the computational error of the algorithm. Based on the results, decisions on further treatment cannot be made because the error for some X-ray images is too large. The results of the algorithm can only help to confirm the progress of treatment that the doctor has established (Table 1).

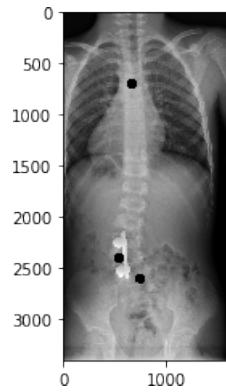


**Figure 1:** Points dividing the spine segments according to the type of scoliosis into subsegments.

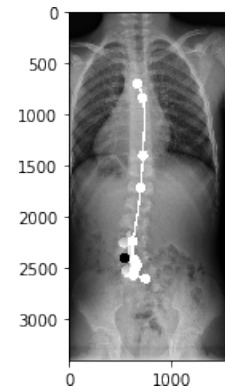


**Figure 2:** Interpolation of the line crossing the start points by 5th polynomial.

**Table 1:** Comparison of the results between the manually measured and calculated Cobb's angle

Patient	Year	Manually measured Cobb's angle	Calculated Cobb's angle	Difference
1	2012	35°	36°	1°
1	2013	29°	31°	2°
1	2015	23°	26°	3°
2	2015	24°	22°	2°
2	2016	21°	18°	3°
2	2017	20°	16°	5°
3	2013	12°	13°	1°
3	2014	8°	5°	3°
3	2016	4°	3°	1°

Cecilie Josefine Mørch Ingkirk (Aarhus University)

***GABAergic system deficit in the prefrontal cortex of Df(h15q13)/+ genetic mouse model of schizophrenia***

*Joint with Abdel-Rahman Al-Absi, Per Qvist, Simon Glerup, Connie Sanchez and Jens R. Nyengaard*

**Introduction:** The 15q13.3 microdeletion is a 1.5 mega-base copy number variation that affects six genes from the human chromosome 15, causing higher risk to develop schizophrenia among other neuropsychiatric disorders. Human carriers of this microdeletion syndrome experience different levels of cognitive dysfunctions; including attention, learning and memory deficits. The GABAergic system is a key regulator of the cognitive functions, therefore GABA deficit might be correlated to the cognitive symptoms of schizophrenia.

**Methods:** A Df(h15q13)/+ model was recently generated to mimic the 15q13.3 microdeletion. Using this model, we investigate the possible GABA deficit in the prefrontal cortex using behavioral, molecular and structural approaches.

**Results:** Df(h15q13)/+ mice displayed visuospatial memory deficit in the object location test. Furthermore, a decrease in the protein levels of GAD65 and VGAT in the PFC of Df(h15q13)/+ mice was detected. However, GABA neurotransmitter levels did not change between genotypes.

**Conclusion:** Results suggest a deficit in the GABA system at the presynaptic level in the prefrontal cortex of Df(h15q13)/+ mice. Further investigations are necessary to correlate these deficits to the other observations from this microdeletion syndrome.

Mia Staal Jensen (Aarhus University)

***Does Olanzapine change Orexin A expression?***

*Joint with Maiken K. Mikkelsen, Connie Sanchez and Jens Randel Nyengaard*

Schizophrenia is a serious mental illness that today is treated with second generation atypical antipsychotic drugs such as Olanzapine. Second generation atypical antipsychotic drugs have a lower incidence of extrapyramidal side effects than the first generation of antipsychotic drugs. Unfortunately, they also have distinct metabolic side effects in up to 80% of treated patients. Numerous studies have investigated the central and peripheral side effects of atypical antipsychotics in rodents as well as humans. The mechanisms underlying the dysmetabolic effects of the atypical antipsychotics are, however, still not fully understood. This study aims to investigate the effects of Olanzapine in the lateral hypothalamus of female rats that have been treated with Olanzapine or vehicle for 2 days (acute). This study is a part of a bigger project investigating Olanzapine's effect on the entire appetite regulating center in the hypothalamic region of the brain.

Immunohistochemistry was used to visualize Orexin A neuropeptides in rat brain sections, cut in 50 µm thick sections and sampled across the entire lateral hypothalamic region. The region of interest, lateral hypothalamus, was delineated in all sections, and a z-axis analysis was performed to test for staining penetration, shrinkage and loss of cells. The number of Orexin A neuropeptide expressing neurons were quantified using the optical fractionator. In addition, Orexin A concentrations in rat plasma has been quantified using competitive enzyme immune assay (EIA). The EIA results revealed that there was no significant difference between Olanzapine and vehicle treated rats. This indicates that peripheral levels of Orexin A are not associated with the dysmetabolic side effects of Olanzapine.

This study will hopefully result in better understanding of the side effects of atypical antipsychotic drugs which can help develop a more specific medical model for Schizophrenic patients using atypical antipsychotic drugs.

Iva Karafiátová (Charles University)

***Statistical aspects of random tessellations with microstructure marks***

*Joint with Zbyněk Pawlas and Luděk Heller*

A random marked tessellation is obtained by attaching a random mark to each cell of a random tessellation. This mathematical model is useful when dealing with 3D polycrystalline materials. The tessellation describes grain microstructure while the marks may describe microstructure morphology parameters or elastic grain interaction parameters. It means that the marks could be categorical or numerical, e.g. grain volumes, grain shape sphericity or numbers of neighbouring grains. However, they could be also more complex, e.g. vectors representing grain orientations or grain-wise averaged stress tensors. Since we are interested in the effect of microstructure parameters on elastic grain interactions, also the combination of above-mentioned marks can be considered.

We investigate dependence between marks and cells of random marked tessellations as well as dependence structure among marks. Two basic approaches are followed. By associating the cell with its center of mass each random marked tessellation naturally generates a marked point process. The first approach is thus based on the analogy of second-order summary characteristics introduced for marked point processes. If the marks have more components we also study dependence structure within marks. In this case, cross-type characteristics are considered. The second approach exploits geostatistical methods developed for random fields. In both approaches, the summary characteristics have to be estimated from data. We present some results of the analysis of NiTi wire microstructure that was reconstructed from 3D-XRD data using the Laguerre tessellation.

Kateřina Koňasová (Charles University, Prague)

***Classification task in the context of replicated point patterns***

*Joint with Jiří Dvořák (Charles University, Prague)*

Classification task, one of the fundamental tasks in machine learning and also in statistics, aims to classify a new observation to the one of the  $k$  possible classes. In the point pattern setting, its purpose is to label the incoming observed pattern with one of the  $k$  possible labels.

For solving the classification task numerous methods are available. Some of them are related with measuring dissimilarities between investigated objects. In the point pattern setting, there exist various metrics that can be used as a dissimilarity measure (e.g. the Hausdorff metric), but most of them ignore some important properties of the underlying point pattern data.

We propose a non-parametric approach to solving the classification task in the context of replicated point patterns using the kernel regression method. In this case we consider a semimetric based on functional summary characteristics as a dissimilarity measure. The employment of functional summary characteristics

could be quite advantageous, since they contain a valuable information about the geometrical structure hidden in the investigated data. Performance of this method will be illustrated by means of simulation study and some examples of the classification task for real point pattern data will be discussed.

Nick Y. Larsen (Aarhus University)

***Characterisation of minicoloumnarity and volume tensors of neurons in Brodmann Area 46 in normal, schizophrenic and depressive human autopsy brains***

*Joint with Eva Bjørn Vedel Jensen, Sun Fei, Grazyna Rajkowska, Jon Sparring and Jens Randel Nyengaard*

Schizophrenia and depression are neuropsychiatric diseases that affect a person's feelings and behaviour. Both mental disorders are influenced by environmental and genetic factors, which leads to social problems for the individual patient, family and friends as well as economic costs for the society. fMRI and PET studies have shown abnormal activation of the dorsolateral prefrontal cortex (DLPFC) in Brodmann Area 46 (BA46), which is involved in the development of schizophrenia and depression.

This could be due to an altered 3-dimensional size, orientation, shape and organization of the neurons in BA46. Using autopsy human brains from 11 control subjects, 10 subjects with schizophrenia, 11 suicidal patients with a history of depression, and 8 subjects with major depression without committing suicide, advanced methods from stochastic geometry and 3-dimensional reconstruction will be implemented for the characterization of minicoloumnarity and volume tensors of neurons in BA46.

BA46 will be identified from thick and thin histological sections and the sampling of cells will be carried out by various forms of optical microscopy and serial sectioning bright field microscopy.

Assuming a difference in number, organisation or orientation of neurons in BA 46 of normal subjects, and patients with schizophrenia or depression, it will be a very significant step in a better understanding of the pathophysiology behind schizophrenia and depression.

Michelle Meier (Aarhus University Hospital)

***Morphological Dynamics of the Regenerative Hepatocyte***

*Joint with Frank Viborg Mortensen, Jens Randel Nyengaard, Stephen Hamilton-Dutoit, Anders Riegels Knudsen and Kasper Jarlhelt Andersen*

**Background:** Malignancy of the liver is one of the primary causes of cancer-related death world-wide. Partial hepatectomy (PH) is first-line curative treatment owing to the unique ability of the liver remnant to regenerate while maintaining

body homeostasis. Depending on the size and functional capacity of the liver remnant, deterioration of function can lead to post-hepatectomy liver failure. Therefore, if malignancy is widespread in the liver, the size of PH and, hence, the size of the liver remnant may limit curability. The overall aim of this study was to investigate and characterize the impact of different sizes of PH with regard to the rat liver regenerative process. Specifically, for results presented here, we wanted to investigate the morphological dynamics of the regenerating hepatocyte (hypertrophy and proliferation) assessed by stereology.

**Materials and Methods:** In a rat model of 30%, 70%, and 90% PH together with a group of sham-operated and non-operated rats, the following were investigated at post-operative days (POD) 1, 3, and 5: hepatocyte volume and hepatocyte proliferation together with liver-specific biochemistry and regeneration ratio.<sup>1</sup>

Hepatocyte volume was estimated using immunohistochemical staining for the hepatocyte cell membrane-proteine  $\beta$ -catenin, involved in cell-cell adhesion and localized to the cell membrane in normal cells ([1]). The object of interest (OI) was hepatocytes with a clear  $\beta$ -catenin-stained cell membrane and a counterstained oval nucleus. The planar rotator was used for estimation ([2]). The procedure is described briefly in Figure 1. The mean hepatocyte volume in a section ( $V_{\text{mean}}$ ) was calculated using the following equation (1):

$$V_{\text{mean}} = 10^{V_{\text{mean}}(\log(V_i))} \quad (1)$$

$V_{\text{mean}}(\log(V_i))$  = a logarithmic calibrating constant

$$= \sum_i \log\left((V_i) \times \left(\frac{t_i/h_{\text{dis}}}{\sum_j (t_j/h_{\text{dis}})}\right)\right),$$

$V_i$  = the individual hepatocyte volume,  
calculated by the NewCast software,

$t_i$  = the section thickness = 30  $\mu\text{m}$ ,

$h_{\text{dis}}$  = 12  $\mu\text{m}$ .

---

<sup>1</sup>A percentage estimate of the actual size (wet weight) of the liver remnant relative to the estimated liver weight prior to PH to evaluate the increase in liver size (weight) in the postoperative period after PH.

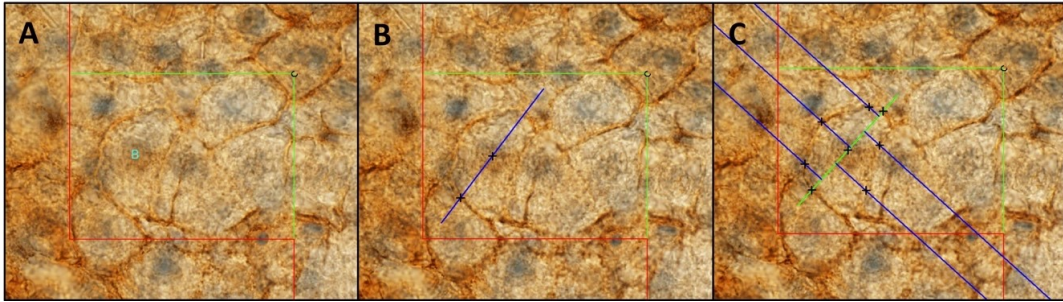


**Figure 1:**  $\beta$ -catenin stained section presenting the steps measuring the hepatocyte volume by the planar rotator [2]. CF is displayed and the above described counting rule was followed, the OI being hepatocytes with a clear  $\beta$ -catenin stained cell membrane (dark-red) and a counterstained (gray) oval nucleus in focus. The planar rotator was applied as follows: **A:** Through the middle of the nucleus the longest axis of the hepatocyte was marked (“B” in the picture indicating that this hepatocyte is counted). **B:** Intersections between the longest axis and the hepatocyte cell-membrane were marked, defining the cell “height”. **C:** The software generated uniform, random, and parallel test-lines perpendicular to the longest hepatocyte cell axis and intersections between these test lines and the hepatocyte cell membrane were marked, defining the distance of the intercepts at both sides of the axis. In each section, a mean of 25 CFs ( $75 \mu\text{m} \times 55 \mu\text{m}$ ) and an average of 50 hepatocytes were sampled for hepatocyte mean volume estimation. The figure was published by M. Meier et al. [3].

*Hepatocellular proliferation* was estimated using immunohistochemical staining for the Ki-67 antigen. Ki-67 is a protein located in the nucleus and exclusively present in proliferating cells [4, 5]. The object of interest (OI) was Ki-67-positive stained nuclei of the hepatocytes. The optical fractionator method was used for estimation [6]. The procedure is described briefly in Figure 2. The total number of proliferating hepatocytes ( $N$ ) of the posterior caudate lobe was calculated using the following equation (2):

$$N = \frac{1}{\text{SSF}} \times \frac{1}{\text{ASF}} \times \sum Q^- \quad (2)$$

$$\text{SSF} = \text{section sampling fraction} = \frac{\text{BA}}{\text{mean}(t_{\text{slab}})}$$

$$\text{BA} = \text{block advance} = \text{the height of the sampled section,} \\ = 30 \mu\text{m}$$

$$\text{mean}(t_{\text{slab}}) = \text{the mean thickness of the embedded slabs after shrinkage} \\ = 1784 \mu\text{m} \quad [7],$$

$$\text{ASF} = \text{area sampling fraction} = \frac{a(\text{frame})}{dx \times dy},$$

$$a(\text{frame}) = \text{the area of the two-dimensional unbiased counting frame,} \\ dx \text{ and } dy = \text{the stepping distances in the } x \text{ and } y \text{ directions,}$$

$$\text{HSF} = \text{height sampling fraction} = \frac{h_{\text{dis}}}{\text{mean}(t_{Q^-})},$$

$$h_{\text{dis}} = \text{the disector height} = 15 \mu\text{m},$$

$\text{mean}(t_{Q^-})$  = the Q-weighted mean section thickness,

$\sum Q^-$  = the total count of Ki-67 positive hepatocytes in a section.

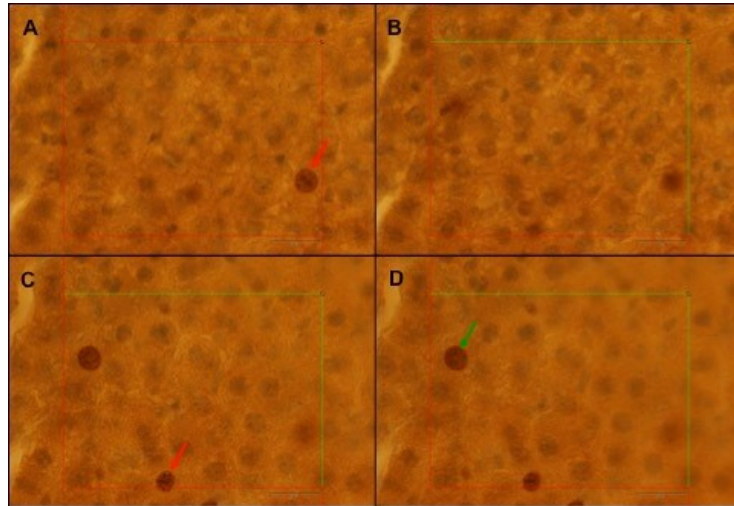


**Figure 2:** Figure 2 Ki-67-stained section presenting four different optical levels (A-D) within the section when focusing the microscope down through the section. The number of proliferating hepatocytes was estimated by the optical fractionator method [6]. The counting frame (CF), the red lines are exclusion lines, and green lines are inclusion lines. Following the universal counting rule [8], the objective of interest (OI) being Ki-67 positive-stained hepatocyte nuclei (Ki-67pos) were counted if they were entirely contained within the CF or if they touched an inclusion line without touching an exclusion line. **A:** Inactive CF – Ki-67pos not included (NI) (red arrow). **B:** Active CF – Ki-67pos not in focus, therefore NI. **C:** Active CF – Ki-67pos touches exclusion line, therefore NI. **D:** Active CF – Ki-67pos entirely contained within the CF, therefore included in the count (green arrow). A minimum of 100 positive cells had to be counted per section to maintain statistical significance. Therefore, prior to the counting-process each section was grouped according to an overall valuation of the number of positive hepatocytes in the section: Few Ki-67pos → number of CFs: 120. Moderate number of Ki-67pos → number of CFs: 50. Numerous Ki-67pos → number of CFs: 25. The figure was published by M Meier et al. [9].

**Results:** Overall, the dynamics and the molecular biological response of liver regeneration were highly dependent on the extent of the PH. Of special interest was the dynamics following PH(90%), biochemically presenting with post-hepatectomy liver failure at POD1 (very low prothrombin-proconvertin ratio and extremely elevated bilirubin and ammonia). Although in a critical state, the regeneration rate following PH(90%) increased immediately after surgery, reaching almost 100% at POD5. The hypertrophic dynamics after PH(90%) followed that of the less extensive PHs, with an early volume increase and peak at POD1, more pronounced the more extensive the PH (Fig. 3A). Likewise, the proliferative response to PH(90%) was most pronounced, although delayed (Fig. 3B). The results are summarized in Figure 3C.

## Abstracts for posters

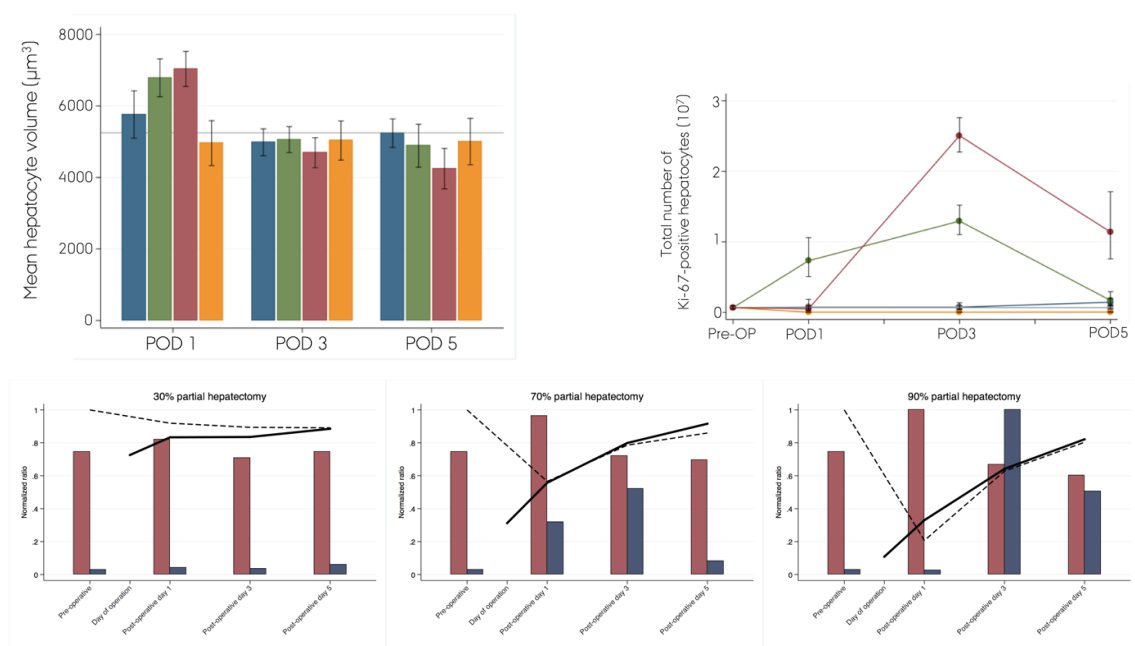


**Figure 3:** Figure 1 **A:** Mean hepatocyte volume by size of partial hepatectomy. **B:** Total number of Ki-67-positive hepatocytes in the posterior caudate rat liver lobe (median). Blue: PH(30), green: PH(70), red: PH(90), orange: sham, gray: baseline. 95% CI. **C:** Hypertrophy and proliferation of the hepatocytes normalized to the maximum potential (90%PH POD1 resp. POD3) in relation to the regeneration rate and liver function (PP) by size of hepatectomy pre- and postoperatively. Red bar: normalized mean hepatocyte volume, blue bar: normalized number of Ki-67 positive hepatocytes, black line: regeneration rate, dashed line: prothrombin-proconvertin ratio (normalized to baseline). The figures were published by M Meier et al. [9, 3].

**Conclusion:** Although in a critical state of post-hepatectomy liver failure, the hypertrophic dynamics after extensive PH(90%) follows that of less extensive PHs, with an early volume increase and peak at POD1, which is more pronounced the larger the PH. Yet, the proliferative response to PH(90%) is delayed, proposedly as a consequence of the early condition of post-hepatectomy liver failure.

*The above-presented studies and results were part of the PhD thesis “The morphological and molecular biological response to partial hepatectomy and regeneration in rats” from 2019, by M. Meier.*

### References

- [1] Ozawa M, Baribault H, Kemler R. The cytoplasmic domain of the cell adhesion molecule uvomorulin associates with three independent proteins structurally related in different species. *EMBO J.* 1989;8:1711–1717.
- [2] Rasmusson A, Hahn U, Larsen JO, Gundersen HJG, Jensen EBV, Nyengaard JR. The spatial rotator. *J Microsc.* 2013;250:88–100.
- [3] Meier M, Andersen KJ, Knudsen AR, Nyengaard JR, Hamilton-Dutoit S, Mortensen FV. Adaptive growth changes in the liver remnant are affected by the size of hepatectomy in rats. *Int J Exp Pathol.* 2018;99:150–157.

- [4] Scholzen T, Gerdes J. The Ki-67 protein: From the known and the unknown. *J Cell Physiol.* 2000;182:311–322.
- [5] Gerlach C, Sakkab DY, Scholzen T, Daßler R, Alison MR, Gerdes J. Ki-67 expression during rat liver regeneration after partial hepatectomy: Ki-67 expression during rat liver regeneration after partial hepatectomy. *Hepatology.* 1997;26:573–578.
- [6] Gundersen HJG. Stereology of arbitrary particles. *J Microsc.* 1986;143:3–45.
- [7] Andersen KJ, Knudsen AR, Kannerup A-S, et al. Sorafenib inhibits liver regeneration in rats. *HPB.* 2013;15:944–950.
- [8] Gundersen HJG. Notes on the estimation of the numerical density of arbitrary profiles: the edge effect. *J Microsc.* 1977;111:219–223.
- [9] Meier M, Andersen KJ, Knudsen AR, Nyengaard JR, Hamilton-Dutoit S, Mortensen FV. Liver regeneration is dependent on the extent of hepatectomy. *J Surg Res.* 2016;205:76–84.

Maiken K. Mikkelsen (Aarhus University)

***Does Olanzapine leads to changes in the hypothalamic opioid sytem?***

*Joint with Nick Y. Larsen, Connie Sanchez and Jens Randel Nyengaard*

Antipsychotic medication used for the treatment of schizophrenia is associated with many debilitating adverse effects. Although second generation atypical antipsychotics, such as Olanzapine, has less extrapyramidal side effects, they result in weight gain and metabolic dysfunction in up to 80% of treated patients. In addition, it appears that Olanzapine has different side effect patterns in male and female, with increased fat deposits without weight gain in men, and increased appetite with weight gain in women. Both peripheral and central nervous system effects of Olanzapine have been studied for many years, however, very little is known about the effects on the appetite regulating center hypothalamus. Studies have shown that olanzapine leads to an increase in appetite stimulating RNAs and a decrease in appetite suppressing RNAs in the arcuate nucleus of hypothalamus. We are studying Olanzapine's effect on appetite- and energy regulating neurons of the hypothalamus in female rats. Preliminary results show a significant weight gain and increased food intake after only 72 hours of treatment. To investigate the effect of Olanzapine on opioid receptor expression in the hypothalamus we used fluorescent *in situ* hybridization staining's of rat brain sections, which were subsequently tile imaged at high magnification on a Leica fluorescent microscope. The area of interest were delineated and the number of RNA 'dots' were quantitatively detected determined using a MATLAB script. The results showed that 48 hours of olanzapine treatment results in a decreased expression of  $\mu$  opioid receptor RNA in the arcuate nucleus, a central regulator of appetite in the brain. Studies have shown that the opioid system participates in the regulation of food intake in the hypothalamus, and a new phase III study has found that patients treated with olanzapine and a  $\mu$  opioid receptor antagonist results in less weight

gain. Further experiments are in progress to determine olanzapine driven changes in opioid receptor and serotonin receptor expression in the hypothalamus, as well as estimations on neuroanatomical changes in appetite regulating neuron populations. Knowledge obtained in this study could result in advancing a more specific medical targeting against both the adverse effects caused by atypical antipsychotic treatment, as well as obesity in general.

Rebecca Nyengaard (Aarhus University)

***Quantification of histopathological changes in the inner ear and electrophysiological assessment of hearing function in newborn piglets with hypoxic-ischemic-encephalopathy following perinatal asphyxia***

*Joint with Tommi Anttonen, Jens Randel Nyengaard, Kasper Jacobsen Kyng, Tine Brink Henriksen and Christer Zøylner Swan*

Perinatal asphyxia results in hypoxic-ischemic-encephalopathy (HIE) in 1–6 per 1000 live human births, of which 10%–60% of affected infants die. 30%–100% of the survivors suffer mild to severe systemic and neurologic deficits, including sensorineural hearing loss (SNHL). Previous descriptive histological studies have suggested that perinatal asphyxia-induced SNHL is due to drastic cellular damage occurring in the central and/or peripheral auditory system. However, quantified histopathological evidence of HIE-induced SNHL related to electrophysiological assessment of auditory pathways is limited.

In order to study cellular damage in the inner ear following perinatal asphyxia, we applied a piglet survival model of perinatal HIE. HIE was induced in 15 Danish Landrace <24 h old piglets.

Auditory brainstem response (ABR) was performed pre- and post-asphyxia to evaluate auditory pathway function and will be correlated to cellular changes in the inner ear and central pathways. The severity and tonotopical distribution of cellular damage will be determined based on morphological and immunohistochemically related signs of cell death on virtual slides from the inner ears of the piglets by using the physical fractionator. Total hair cell number will be quantified using the optical fractionator. Our results seek to determine the extent to which inner ear damage in perinatal asphyxia contributes to early risk assessment of patients in risk of developing SNHL following perinatal asphyxia.

Mikkel V. Olesen (Bispebjerg and Frederiksberg Hospital)

***Pathological changes in the cerebellum of patients with Multiple System Atrophy and Parkinson's disease***

*Joint with Elisabeth H. Lynnerup Rusholt, Lisette Salvesen, Tomasz Brudek, Betel Tesfay and Bente Pakkenberg*

Multiple System Atrophy (MSA) and Parkinson's disease (PD) are synucleinopathies characterized by aggregation of  $\alpha$ -synuclein in brain cells. Recent studies have shown that morphological changes in terms of cerebral nerve cell loss and increase in glia cell numbers, the degree of brain atrophy and molecular and epidemiological findings are more severe in MSA than PD.

In the present study, we used Cavalieri's method, optical disectors and the rotator to quantify cerebellar volumes, the total number of granule- and Purkinje cells, and the mean volume of Purkinje cell perikarya and nucleus in cerebellar subregions of nine patients diagnosed with MSA, 10 PD patients and 15 age-matched control subjects.

Only brains from MSA patients displayed a reduction in the total number of Purkinje cells and Purkinje cell volumes (perikaryons and nuclei volume), while a reduction in the white matter volume was observed in both MSA and PD brains, compared to controls. The number of granule cells was unaffected in both diseases. Analyses of cell type-specific mRNA expression supported our structural data.

This study of the cerebellum is in line with previous findings in the cerebrum and demonstrates that the degree of morphological changes is more pronounced in MSA than PD. Further, our results support an explicit involvement of cerebellar Purkinje cells and white matter connectivity in MSA and points to the potential importance of white matter alterations in PD pathology.

Estrid Thougard Pedersen (RLSN, Bispebjerg and Frederiksberg Hospital)

***Identifying structural endophenotypes in a rat model of schizophrenia-like behavior***

*Joint with Ana Sanchez-Gonzalez, Adolf Tobeña, Bente Pakkenberg, Alberto Fernandez-Teruel and Susana Aznar*

Animal models reflecting cognitive manifestations of mental disorders are widely used to shed light on the neurobiology behind specific behavioral phenotypes. The Roman rat strains are a neurobehavioral animal model derived from selective breeding into an inbred Roman Low- (RLA-I) and Roman High-Avoidance (RHA-I) strain, based on their performance in the two-way active avoidance task in the shuttle box. The RHA-I strain presents behavioral phenotypes associated with schizophrenia and schizophrenia risk, making it an ideal model for investigating the underlying neurobiology behind these behavioral traits. The prefrontal cortex (PFC) is a central player in cognitive processes, which are known to be impaired

in schizophrenia. Interestingly, the RHA-I strain, when compared to the RLA-I, show enhanced expression of pre- and postsynaptic components and increased number of immature dendritic spines in this region. The aim of this study is to investigate whether this is accompanied by differences in number of astrocytes and microglia, as these cells are involved in regulating synaptic pruning.

Coronally cut brain sections from male RHA-I ( $n = 5$ ) and RLA-I ( $n = 5$ ) rats were stained for GFAP and Iba1 for identification of astroglia and microglia respectively, using colorimetric immunohistochemistry. The optical fractionator sampling design was used to estimate the total numbers of astrocytes and microglia in mPFC, and a point-counting method based on Cavalieri's principle in combination with systematic random sampling was used to estimate the reference volume of mPFC.

RHA-I rats had a significantly higher number of astrocytes in their mPFC than their RLA-I counterparts ( $P \leq 0.01$ ). The number of microglia in mPFC did not differ between the two groups, neither did the volume of the mPFC.

The finding that astrocyte numbers in mPFC is increased in RHA-I rats is in line with findings from other studies of animal models of schizophrenia and psychosis, as well as in schizophrenic patients, where changes in astrocyte numbers have been observed in different brain regions. The astrocytes might therefore be involved in the synaptic alterations and cognitive deficits observed in the RHA-I rats.

Ellen Lund Schaldemose (Aarhus University Hospital)

***Evaluation of Corneal confocal microscopy images in patients with type 1 diabetes and diabetic polyneuropathy: a stereological reappraisal***

*Joint with Rasmus Eich Hammer, Jens Randel Nyengaard and Pall Karlsson*

**Introduction:** Corneal confocal microscopy (CCM) is a non-invasive clinical method to analyse and quantify corneal nerve fibres in vivo and thereby small fibre neuropathy (SFN), e.g. diabetic polyneuropathy. The CCM-technique is in constant progress, but there are methodological limitations in terms of sampling of images and objectivity of the nerve quantification. We have previously developed and described a new randomized sampling method in an adjusted area dependent image analysis of the CCM-images assessing these limitations. Compared to the most common, but subjective used sampling method, this new method found a reduction in nerve fibre length density. This diversity indicates the importance of clear guidelines for the image sampling and the importance of improving the analysis of the CCM images. The gold standard of assessing SFN is the skin punch biopsy. The aim of this study was to test the new sampling method and adjusted volume calculation, on already published data on CCM and skin biopsy from diabetic polyneuropathy patients and healthy controls.

**Methods:** All ccm-images from 26 control subjects and 63 patients with type 1 diabetes from an already published article were included. The images were randomly selected using the new method and corneal nerve fibre length density

(CNFL), corneal nerve fibre branch density (CNBD) and corneal nerve fibre density (CNFD) were determined in both a manual and automatic manner. The CCM measures between the two methods were compared and correlational analysis between the CCM measures and skin biopsies was performed.

**Results:** The study is still ongoing, but preliminary data suggest a reduction in CNFL, CNBD and CNFD using the new sampling method compared with the common used method. Results on skin biopsy are not yet analyzed. The final results will be presented at the meeting.

**Conclusion:** The preliminary results suggest that using more objective sampling and area-adjusted analysis of CCM images results in lower measures and therefore an overestimation when using the common sampling method.

Maria Søndergaard Thøfner (University of Copenhagen)

***Superficial dorsal horn volume loss in dogs with neuropathic pain and syringomyelia – a quantitative and qualitative histological characterisation of cervical spinal cord lesions***

*Joint with Troels Staehelin Jensen, Jørgen Steen Agerholm, Ole Jannik Bjerrum, Mette Berendt and Jens Randel Nyengaard*

**Background and aim:** Syringomyelia give rise to central neuropathic pain (CNeP) in humans as well as dogs of the breed Cavalier King Charles Spaniel (CKCS). A correlation between symptoms and magnetic resonance imaging (MRI) findings (syrinx dimension, syrinx / spinal cord ratio and degree of syrinx asymmetry) has been established in both humans and dogs. However, descriptions of histomorphological characteristics and their association with symptoms of central neuropathic pain in humans and dogs with syringomyelia are sparse. We hypothesise that CKCS with syringomyelia-related signs of CNeP represent a spontaneous model of CNeP. In order to characterise this translational model, we aimed to quantify and describe the neurohistopathological lesions in the cervical spinal cord. In this study we investigated (1) a possible relation between symptoms and volume loss of a specific anatomical entity involved in nociception and (2) if syringomyelia affected specific functional spinal cord units of nociception.

**Methods:** Private owned CKCS with a well-characterised pain phenotype and MRI-confirmed syringomyelia ( $n = 8$ ) and asymptomatic controls ( $n = 4$ ) were included. The dogs were donated by their owners after euthanasia. Spinal cord segments C1–C8 were sampled, formalin-fixed and paraffin-embedded. Serial 30  $\mu\text{m}$  sections were stained with haematoxylin-eosin, luxol fast-blue (myelin) and thionine (nuclei) for neurohistopathological characterisation. 10  $\mu\text{m}$  sections were stained with a neurofilament triplet H protein-specific primary antibody (SMI-32) to delineate the dorsal horns' laminae I-III as a representation of spinothalamic neurons after systematic random sampling. The block sampling fraction was 1:2. Volumes of specific anatomical entities (the central canal, syrinx – if present, left

and right dorsal horns' laminae I-III, the remaining left and right grey matter and dorsal, lateral and ventral white matter columns) were estimated using the 2D nucleator and the Cavalieri estimator.

**Results:** Paired comparison of total volumes of the specific anatomical entities between the affected and non-affected halves of the spinal cord in cases with lateralised clinical signs of CNeP ( $n = 7$ ) was undertaken. A significant volume loss of the dorsal horn laminae I-III was found on the affected side to which the clinical signs were ascribed:  $34 \mu\text{m}^3$  (range 20–48) compared to the non-affected side,  $42 \mu\text{m}^3$  (range 27–54,  $P = 0.034$ ). In the spinal cord segment most significantly affected by syringomyelia, the mean reduction in dorsal horn area on the affected side was 56% (range 8%–95%) compared to the contralateral, non-affected dorsal horn area. The remaining comparisons revealed non-significant differences between affected and non-affected sides. Unpaired comparisons of the total mean volumes of the spinal cord and sub-volumes revealed no significant differences between cases and controls. No histopathological abnormalities were found in the asymptomatic controls' spinal cords. A clear pattern of ipsilateral changes in the dorsal root entry zone characterised by deafferentation and reorganization of first-order axons into deeper laminae was found in cases with lateralised clinical signs.

**Conclusions:** Syringomyelia in CKCS with clinical signs of CNeP primarily affects the spinal cord grey matter. The loss of dorsal horn grey matter and dorsal root entry zone pathology are neurohistopathological characteristics shared with human syringomyelia patients. The neurohistopathological findings confirm the back- and forward translational potential of this spontaneous model to fill the gap between induced rodent models and human patients. Establishing the causal relation between syringomyelia and CNeP in the CKCS will further strengthen this spontaneous model's translational potential.

Markéta Zikmundová

*Covering of the realisations of the random sets*

In recent years, random sets were recognised as a valuable tool in modelling different processes from fields like biology, biomedicine or material sciences. Although being able to describe a particular model, sometimes it is enough to distinguish between two realisations without specifying the underlying processes. However, since the realisations can be of very rough shapes, a simplification is usually needed. It may be based on different approximations or covering by simpler objects like discs or other convex compact sets. This poster introduces such simplifications, mentions their advantages and disadvantages, and briefly describes their usage for distinguishing between random sets realisations.